Journal of Environmental Chemical Engineering 13 (2025) 118470

Contents lists available at ScienceDirect

Journal of Environmental Chemical Engineering

journal homepage: www.elsevier.com/locate/jece

Engineering of *Foeniculum vulgare* with material science: La_2O_3-CeO_2-CuO nanocomposites to revolutionize photocatalysis and antimicrobial challenges

Sana Batool [a], Iftikhar Ahmed [b], Calvyn Howells [b], Muhammad Saqib Saif [e], Tuba Tariq [e], Muhammad Waqas [a], Li Haitao [c,d], Yanjun Duan [c,d], Mumtaz Hussain [g], Mansour Ghorbanpour [h], Ghazala Mustafa [f,*], Murtaza Hasan [a,c,d,**]

[a] Department of Biotechnology, Faculty of Chemical and Biological Sciences, The Islamia University of Bahawalpur, Bahawalpur 63100, Pakistan
[b] Environmental and Public Health Department, College of Health Science, Abu Dhabi 11 University, P.O. Box 59911, Abu Dhabi, United Arab Emirates
[c] Nanjing University of Forestry and Technology, Nanjing, 210037, China
[d] National Provisional joint Engineering Research Center of Biomaterials, Nanjing Forestry University, Nanjing 210037, China
[e] Department of Biochemistry, Faculty of Chemical and Biological Sciences, The Islamia University of Bahawalpur, Bahawalpur 63100, Pakistan
[f] Department of Plant Sciences, Faculty of Biological Sciences, Quaid-i-Azam University, Islamabad 45320, Pakistan
[g] Department of Anatomy and Histology, The Islamia University of Bahawalpur, Bahawalpur 63100, Pakistan
[h] Department of Medicinal Plants, Faculty of Agriculture and Natural Resources, Arak University, Arak 38156-8-8349, Iran

ARTICLE INFO

Keywords:
Nanocomposite
Green synthesis
Antimicrobial activity
Photocatalysis
Methylene blue

ABSTRACT

The growing awareness of green avenues and the use of environmentally friendly technologies for crafting nanostructures leads to a remarkable shift in the fabrication approach. In this scenario, developing a highly crystalline heterojunction catalyst based on metal oxides is seen as a promising strategy. This study investigated the synthesis of nanocomposite La_2O_3-CeO_2-CuO and pure La_2O_3, CeO_2, CuO employing *Foeniculum vulgare* as a plant extract. The fabricated samples are characterized by X-ray diffraction (XRD), Fourier-Transform Infrared Spectroscopy (FTIR), Ultraviolet–Visible Spectroscopy (UV-Vis), Transmission Electron Microscopy (TEM), and Energy Dispersive X-ray Analysis (EDAX). The La_2O_3-CeO_2-CuO nanocomposite exhibits remarkable activity against *Escherichia coli* and *Staphylococcus aureus* with activity index and zone of inhibition of 93 % (31.90 ± 0.15 mm), and 92.33 % (27.7 ± 0.12 mm), respectively. Surprisingly, La_2O_3-CeO_2-CuO has a lower band gap, e^-/h^+ recombination, and enhanced charge transfer capability than pure La_2O_3, CeO_2, and CuO. The photodegradation efficiency of La_2O_3-CeO_2-CuO was recorded at 99.7 % after 100 min under sunlight radiation against methylene blue (MB), which was significantly higher than pure La_2O_3, CeO_2, and CuO. Our findings reveal that the La_2O_3-CeO_2-CuO nanocomposite is a highly effective antibacterial agent and photocatalyst formed in conjunction with *Foeniculum vulgare* as a plant extract. The bi-functionality of La_2O_3-CeO_2-CuO holds significant potential in achieving the ultimate clean environment.

1. Introduction

Nanomaterials are in the limelight because of their superior qualities over their bulk counterparts, which include more active sites, and a higher contact surface area. This is part of the hunt for materials that may satisfy society's expanding requirements [1–3]. Materials in the nano and small sizes are having an impact on photocatalytic, pharmaceutical, and medical applications [4–6]. Their applications are growing, including as antimicrobials, contrast agents for imaging, and supports for the effectiveness of drugs and catalysts in breaking down harmful dyes [7–10].

Industrial pollution and microbial infections are serious risks to public health across the globe and are a major cause of death rates. Over a million people are thought to die each year as a result of *S. aureus* and *E. coli*, two of the most common bacteria that cause infection-related mortality. The proliferation of these bacteria is made more

* Correspondence to: Department of Biosciences, QAU, Islamabad, Pakistan.
** Correspondence to: Department of Biotechnology, IBBB, Pakistan.
E-mail addresses: mghazala@qau.edu.pk (G. Mustafa), murtaza@iub.edu.pk (M. Hasan).

https://doi.org/10.1016/j.jece.2025.118470
Received 29 April 2025; Received in revised form 30 July 2025; Accepted 3 August 2025
Available online 5 August 2025

detrimental by unclean surroundings and a lack of access to clean water, which may result in serious illnesses, including sepsis, infections of the digestive tract, and antibiotic resistance [11–13]. Pathogenic microorganisms can spread infections, migrate over massive distances, and create biofilms to increase pathogenicity in the human host [14]. It is the basis of diverse infectious diseases, including pyomyositis, endocarditis, bacteremia, osteomyelitis, cholera, lethal pneumonia, giardiasis, and infections of the skin and soft tissues [15,16]. Furthermore, industrial pollution introduces hazardous compounds that deteriorate water quality and pose long-term health hazards, especially from dye effluents. Organic pollutants, especially dyes, pose a serious threat to the environment because of their "high toxicity, stability, and capacity to cause mutations and cancer." Because it contains methyl bromide molecules, methylene blue, which is extensively utilized in textile manufacturing, is especially hazardous because of its toxicity and stability. It is essential to remove these substances from water to protect aquatic life and water resources from environmental hazards [17,18].

The combination of toxic pollutants and microbiological pollution highlights the urgent need for better public health interventions, more stringent environmental restrictions, and comprehensive water management measures to reduce the hazards implicated [19]. Using metal oxides to create new nanomaterials with dual uses as an antibacterial agent and photocatalyst is a widely recognized area of research [20]. The dynamic potentials of the nanocomposite made it possible to improve the characteristics of existing materials due to its ease of synthesis, size, shape, and doping with a wide variety of metal and non-metal materials at different concentrations [21]. Novel and effective nanocomposites that can function as biological agents to lessen the lethal impact of infectious bacteria and as photocatalysts for purifying water have been created and documented [22]. To obtain unique capabilities for biomedical and environmental applications, researchers and scientists are now working to produce superior, environmentally benign, multifunctional, nanostructure with sustainable qualities [23].

In this situation, tailored metal oxides (MO) are regarded as a significant class of materials that function as antibacterial and photocatalysts [24,25].From the literature inspection, researchers have synthesized effective photocatalysts and antimicrobial agents like $CuO–Co_3O_4$ [26], Zn/Ce–CuO [27], ZnO/SnO_2-CeO_2/CuO [28], $La_2Ti_2O_7$ [29], La_2O_3/CeO_2 [30], La_2O_3–CuO [31], $TiO_2@CeO_2$ and $CeO_2@TiO_2$ [32], $CeO_2/BiVO_4$/g-C_3N_4 [33], Bi_2O_3/CeO_2 [34], TiO_2–Y_2O_3–V_2O_5 [35], CeO_2/CdO [36]. Hence, nanocomposites with widespread applications are significant in biological and environmental research fields that can offer effective catalytic sites for functioning. Among them, La_2O_3, CuO, and CeO_2 stand out owing to their distinctive structural and electrical features. CeO_2, an n-type semiconductor with a bandgap of roughly (~3.26 eV), is well-renowned for its excellent optical, chemical, antibacterial, electronic, and photocatalytic capabilities [37,38]. CuO, a p-type nanomaterial with a small bandgap (~1.20 eV), is widely recognized for its strong antibacterial activity and outstanding photocatalytic efficiency under visible light [39,40]. La_2O_3, with its intermediate bandgap (~4.5 eV), also exhibits antimicrobial potential while enhancing catalytic activity. However, regardless of outstanding features, these materials confront obstacles such as fast electron-hole recombination and restricted solar absorption owing to their bandgap restrictions [41]. The evolution of nanocomposites by combining narrow bandgap semiconductors (CuO) with wide bandgap materials (La_2O_3 and CeO_2) is an effective way to overcome these limitations [42]. It extends the absorbing capacity of solar light toward the visible spectrum, thereby improving catalytic efficiency through reduced recombination and improved charge separation [43,44].

One of the significant medicinal plants used in conventional medicine is *Foeniculum vulgare* [45]. Due to its numerous applications in the food, pharmaceutical, and health cosmetics industries, *Foeniculum vulgare* is currently grown on a large scale in most parts of the world, including southern and central Europe, Asia, many African nations, Brazil, and Argentina [46]. Belonging to the Umbelliferae family, the plant *Foeniculum vulgare* is a popular zing and traditional remedy for a variety of ailments, including liver discomfort, gonorrhea, kidney stones, diaphoretic, fever, insomnia, renal issues, mouth ulcer, laxative, diuretic, Nosebleeds, and stomachache. Ketones, lignin, flavonoids, fiber, protein, saponins, carbohydrates, and vitamins are all abundant in the plant [47]. Because of this, it may potentially be investigated as a possible templating agent for La_2O_3, CeO_2, CuO, and La_2O_3-CeO_2-CuO synthesis.

The addition of bioactive compounds from *Foeniculum vulgare* further increases the nanocomposite's biopotential, making it an extremely effective candidate for environmental and biomedical applications. The synergistic interaction between these materials also improves antibacterial performance and increases pollutant degradation. In this work, we have fabricated a La_2O_3-CeO_2-CuO nanocomposite and systematically investigated it. To evaluate the photocatalytic activity of the La_2O_3-CeO_2-CuO nanocomposite, the photocatalytic degradation of Methylene Blue was used as a model reaction. A variety of parameters were used to evaluate the catalyst. Gram-positive (*Staphylococcus aureus*) and gram-negative (*Escherichia coli*) bacteria were used to elucidate the antibacterial activity of the fabricated La_2O_3-CeO_2-CuO nanocomposite. It offers substantial environmental implications to prevailing circumstances arising due to pathogenic bacteria and toxic pollutant draining into our ecosystem. The synergistic dual behavior of La_2O_3-CeO_2-CuO nanocomposite with tailored properties effectively degrades the harmful pollutants and destroy microbial colonies. Ultimately, this La_2O_3-CeO_2-CuO fabricated by *Foeniculum vulgare* delivers a pathway for cleaner water resources and better human health.

2. Methodology

2.1. Materials

All chemicals and reagents used in the experimentation were of analytical grade without any additional purification. Lanthanum nitrate hexahydrate ($La(NO_3)_3 \cdot 6H_2O$), Cerium nitrate hexahydrate ($Ce(NO_3)_6 \cdot 6H_2O$), and Copper nitrate hexahydrate ($Cu(NO_3)_2 \cdot 6H_2O$), Sodium hydroxide (NaOH) precursor salts used for the synthesis of the samples. Every chemical was purchased in a commercial grade (Sigma Aldrich) and was utilized accurately without any modifications. The entire chemicals used in the present research was 99 percent pure. Moreover, distilled water (DW) was used during the studies. In addition, organic pollutants employed in this study are Methylene Blue dye in the photodegradation test.

2.2. Collection and preparation of plant extract of Foeniculum vulgare

Foeniculum vulgare is taken from the native area of Bahawalpur, PAKISTAN. Fresh plant material, including fennel seeds, leaves, stems, and roots thoroughly washed and dried in a shaded area. Grind the dried plant material by using a pestle and mortar into a fine powder. Mix a 10 g measured amount of *Foeniculum vulgare* powder with 100 mL of water in a 1:10 ratio (w/v). Heat the mixture at 75–85°C for 40–70 min and allow it to stand for a few minutes at room temperature for cooling purposes. Allow the extract mixture to pass through a fine mesh, and the obtained extract solution is filtered through using Whatman filter paper. Store the plant filtrate in a clean, airtight reagent storage bottle at 4°C for further utilization.(Fig. 1)

2.3. Preparation of Foeniculum vulgare assisted La_2O_3–CeO_2-CuO nanocomposites

The synthesis process in brief of La_2O_3, CeO_2, CuO, and La_2O_3–CeO_2-CuO nanocomposites using the analogous experimental conditions was previously discussed in the literature [48]. In three separate reagent bottles, 80 mL of distilled water was combined with 0.01 M of the corresponding salts of lanthanum nitrate hexahydrate, cerium nitrate

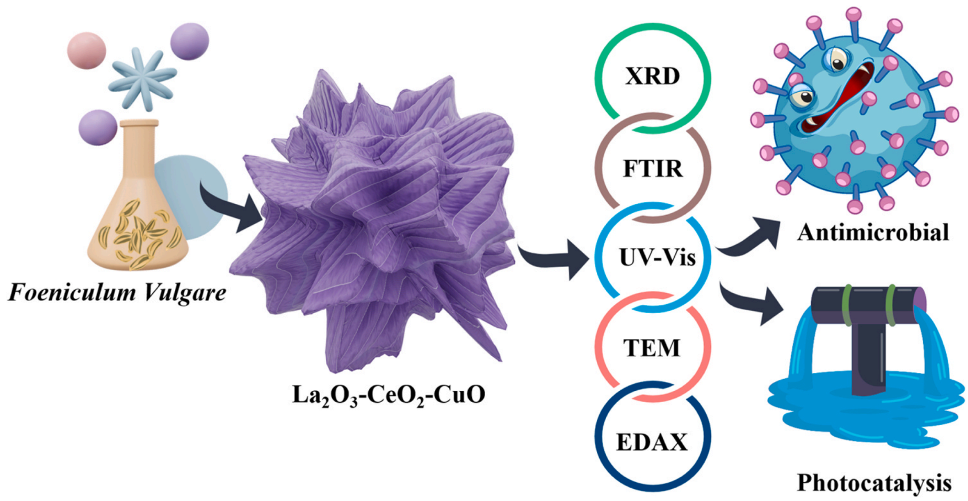

Fig. 1. Graphical representation of La_2O_3-CeO_2-CuO.

hexahydrate, and copper nitrate hexahydrate to create a standard procedure for preparing La_2O_3, CeO_2, and CuO oxides. For fabricating the La_2O_3–CeO_2-CuO nanocomposite, the calculated amount with a molar ratio of **0.5:0.5:0.5** of each salt was mixed in H_2O. Add 50 mL of plant extract to the individual solution. The solution mixtures of each salt and nanocomposites were vigorously stirred for 30 min to dissolve the salts in water. Later, a freshly prepared NaOH solution was further added to the prepared relevant Salt along with the extract solutions to maintain a pH level of 10. Subsequently, stirring of the reaction mixture is continued for 3 h and 50 min. The reaction mixture was centrifuged for 20 min at 6000 rpm. Washed thoroughly the resultant mixture with ethanol many times to remove undesirable ions, and desiccated at 85 °C for 9 h in a drying incubator. The dried samples were finally La_2O_3, CeO_2, CuO, La_2O_3–CeO_2-CuO annealed in a configurable Muffle Furnace at 650 °C for 2 h duration and crushed into fine powder for characterization [49].

2.4. Photodegradation experiment

The fabricated pristine NPs and nanocomposites were assessed through the photodegradation of organic pollutants under direct visible light irradiation. The reaction was conducted for photocatalysis on October 15, 2024, from 12:00–2:00 p.m. at The Islamia University of Bahawalpur, Pakistan. The pyranometer (Kipp & Zonen CMP-11) assessed the recorded intensity to be between 580 and 602 W/m^2. Before being exposed to light, the 20 mg catalyst was added to 50 mL of a dye-aqueous solution and agitated for 60 min in the dark to generate the adsorption-desorption phenomena. Following exposure to sunlight, 3 mL of the dye solution was taken out at predetermined intervals of 0, 20, 40, 60, 80, and 100 min and analyzed using the ultraviolet (UV) spectroscopy method. The MB absorption wavelengths of the dye were observed in nm. The photodegradation reaction of La_2O_3, CeO_2, CuO, La_2O_3–CeO_2-CuO was evaluated through the following relation [50]:

$$\textbf{Degradation performance}(\boldsymbol{\eta}) = \left[\mathbf{c_o} - \frac{\mathbf{c_t}}{\mathbf{c_o}}\right] \times \mathbf{100} \quad \% \tag{1}$$

C_o is the initial concentration of the Mb dye, and Ct is the concentration of dye at time (t) under solar light irradiation. Different scavenger tests, such as EDTA-2Na, ASC, $AgNO_3$and IPA were added to detect the ROS level that affects the photodegradation of dyes.

2.5. Antimicrobial activity

Antibacterial activity was examined for samples La_2O_3, CeO_2, CuO, La_2O_3-CeO_2-CuO, utilizing the disc diffusion technique. The clinical isolates of bacteria were cultured for a period of 24 h at 37 °C in a medium (nutrient broth). The antimicrobial activity was assessed using a standardized inoculum concentration (OD600 = 0.1, or about 10ˆ8 CFU/mL) against *E. coli* and *S. aureus*. Every experiment was carried out in triplicate under sterile conditions, and to guarantee statistical precision, ± standard deviation (SD) is provided. The samples La_2O_3, CeO_2, CuO, and La_2O_3–CeO_2-CuO were dispersed with distilled water of various concentrations, ranging from 20, 40, and 60 μg/mL. The filter paper disc of size (6 mm) was dipped in the fabricated sample solutions. Standard antibiotic ciprofloxacin (0.2 μg/mL) was used for the activity as a positive control. Nutrient agar solution was prepared in a weighted concentration of 2.85 g/100 mL. After adding 20 mL of nutrient agar to the Petri dishes and letting it firm, 100 μL of the test strain was then transferred to the agar surface. The agar surface was then topped with discs that had been soaked in the sample solutions. The Petri plates were parafilm-sealed and incubated at 37 °C for the entire overnight. After 24 h of incubation, the inhibition zone (ZOI) was calculated [51].

$$\textbf{Activity index}(\%) = \left[\frac{\textbf{Zone of inhibition of sample}}{\textbf{Zone of inhibition of control}}\right] \times \mathbf{100} \tag{2}$$

2.6. Characterization techniques

An Advanced Laboratory diffractometer (Bruker-D8, USA) was used to investigate the crystal structure and phase analysis of the fabricated samples. XRD CuKα was performed with λ = 1.5406 Å, 40 kV/35 mA, and 1°/min with a range of 20–80°. The *Foeniculum vulgare* assisted nanostructure's functional group analysis was examined using FTIR on a Bruker Tensor 27 Spectrometer (Germany) in the range of (400–1000 cm^{-1}). The optical patterns were measured using a dual-beam spectrophotometer (Cary-60 Agilent, USA), which has a UV-Vis range of 300–800 nm. Transmission electron microscope (TEM) using the ThermoFisher (USA), and EDX (USA) was employed for detecting elemental analysis of the La_2O_3, CeO_2, CuO, La_2O_3-CeO_2-CuO.

3. Results and discussion

3.1. Structural properties

The XRD pattern of the pure La_2O_3, CeO_2, CuO, La_2O_3-CeO_2-CuO (Fig. 2). It comprises peaks corresponding to hexagonal La_2O_3 [JCPDS CARD NO.01–083–1344] and space group P-3m1. The diffractogram of La_2O_3 showed peaks at 2θ = 26.12, 29.04, 30.02, 39.54, 46.14, 52.10, 55.34, 56.101 are related to (100), (002), (011), (112), (110), (103),

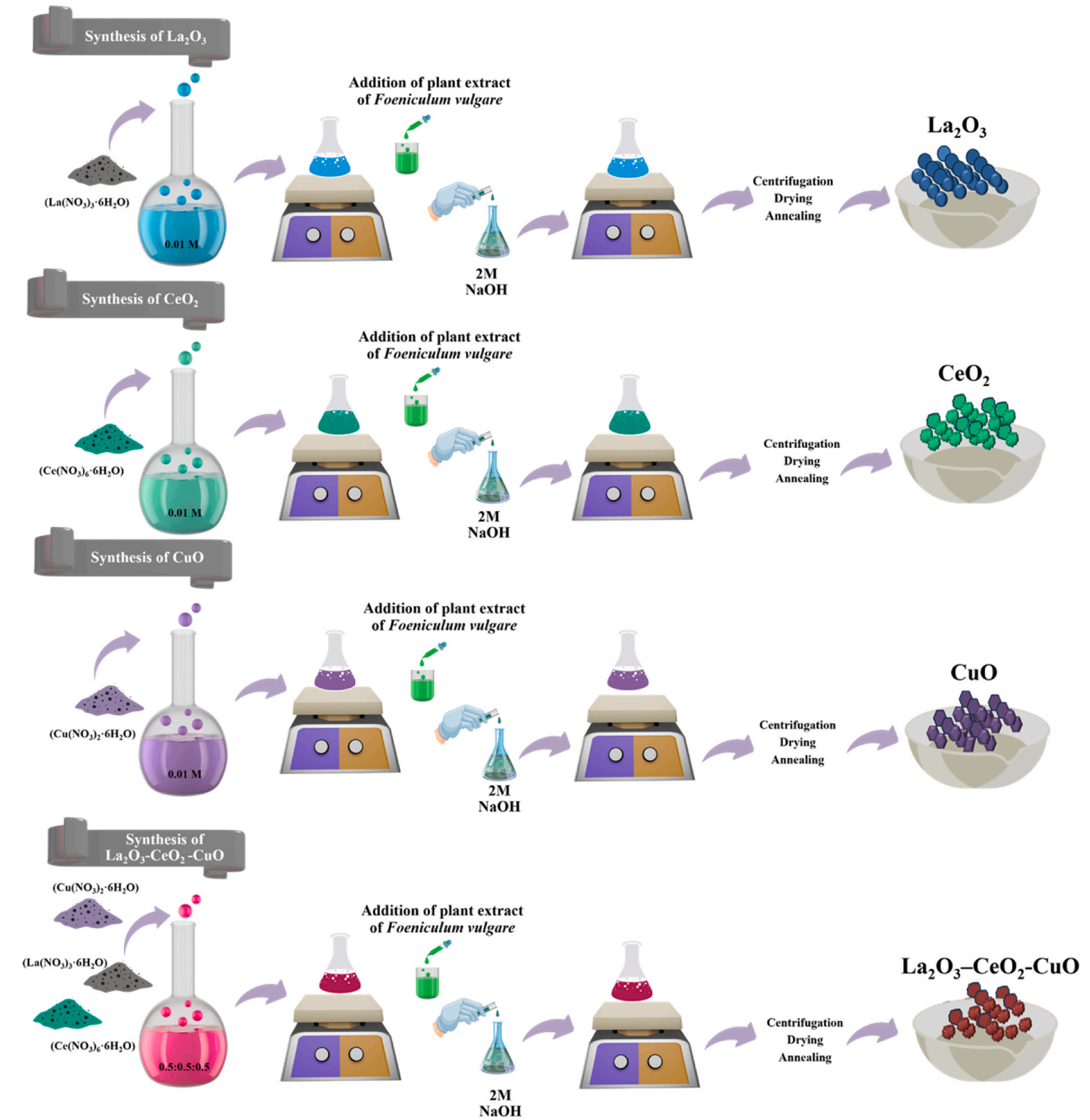

Scheme1. Synthesis Illustration of La_2O_3, CeO_2, CuO, La_2O_3–CeO_2-CuO by *Foeniculum vulgare*.

(112), (201). The corresponding planes and angles of hexagonal La_2O_3 are observed in the spectrum, confirming the synthesis of pure La_2O_3 nanoparticles. The diffractogram of CeO_2 showed peaks at $2\theta = 28.48$, 32.99, 47.34, 56.15, which are related to (111), (200), (220), (311). The CeO_2 spectrum with a cubic crystal system with definite angles and planes confirms the synthesis of pure CeO_2 nanoparticles. It comprises peaks corresponding to cubic CeO_2 [JCPDS CARD NO.03–065–5923] and space group Fm-3m. The diffractogram of CuO showed peaks at $2\theta = 35.54$, 38.82, 48.59, 61.56, 66.13, and 68.12 are related to (-111), (200), (-202), (-113), (-311), and (220). The corresponding planes and angles of Monoclinic CuO are observed in the spectrum, confirming the synthesis of pure CuO nanoparticles. It comprises peaks corresponding to Monoclinic CuO [JCPDS CARD NO.00–005–0661] and space group C2/C. The diffractogram of nanocomposite showed characteristics peaks at $2\theta = 28.54$, 29.64, 35.96, 37.85, 39.66, 47.53, 52.17, 56.43, 61.55 are related to (111), (011), (-111), (111), (012), (220), (103), (311), (-113). From diffractograms, the evaluation of La_2O_3-CeO_2-CuO patterns is crystalline. The nanocomposite resultant peaks relate to hexagonal La_2O_3 [JCPDS CARD NO.01–083–1344], Monoclinic CuO [JCPDS CARD NO.00–005–0661], and cubic CeO_2 with [JCPDS CARD NO.03–065–5923]. The absence of any extraneous peaks in the pure La_2O_3, CeO_2, CuO nanoparticles, and La_2O_3-CeO_2-CuO XRD diffractogram indicates the high purity of crystal growth and deduced values mentioned in (Table S1-S4).(Fig. 3)

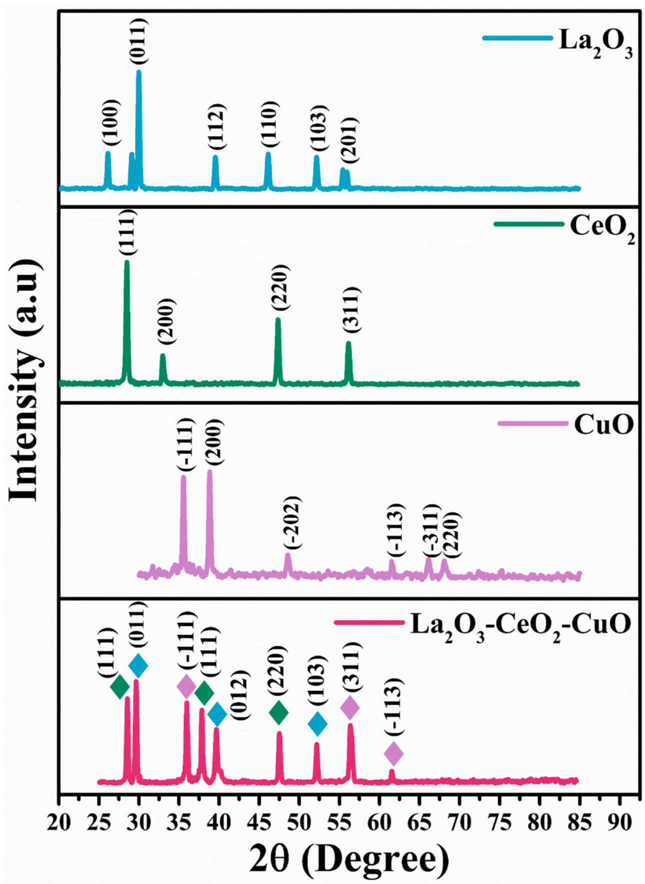

Fig.:2. XRD patterns of *Foeniculum vulgare* assisted La_2O_3, CeO_2, CuO, and La_2O_3-CeO_2-CuO.

Using the Scherrer equation as mentioned in Eq. (3), the crystalline dimension of the produced pristine nanoparticles La_2O_3, CeO_2, CuO, and La_2O_3-CeO_2-CuO nanocomposite was identified [52].

$$\mathbf{D} = \frac{\mathbf{K\lambda}}{\boldsymbol{\beta}\mathbf{cos\theta}} \quad (3)$$

where β is the line broadening at full width at half-maximum (FWHM), which is calculated using a Gaussian single peak fit, D is the average crystal size, K is the constant, λ is the X-ray wavelength, and θ is Bragg's angle. The resulting microstructural parameters are achieved through the derivations mentioned in Table S5.

Fourier transform spectroscopy examines the molecular fingerprint of the materials by highlighting details about the functional groups that comprise the La_2O_3–CeO_2–CuO nanocomposite. The resultant signal encodes all of the infrared frequencies typical of the permitted vibrational modes of the substance under consideration [53]. A reliable technique for analyzing biodegradable and biocompatible polymer nanocomposites is Fourier transform infrared (FTIR). By interpreting the characteristics and dynamics of the material's characteristic vibrational bands, FTIR can detect conformational changes associated with the twisting, stretching, and bending of the polymer chain backbone. FTIR spectra of plant extract of *Foeniculum vulgare* show distinct peaks at 625 cm^{-1} that correspond to aromatic bending C–H groups vibrations [54,55]. The band at 1076 cm^{-1},1376 cm^{-1}, and 1585 cm^{-1} displays a characteristic of stretching and bending vibrations of alcohol and aromatic groups. Another band at 2368 cm^{-1} and 3737 cm^{-1} represent C☰C, C☰N and O-H stretching [56,57]. FTIR spectra of La_2O_3 show distinct peaks at around 678.1036 cm^{-1} assigned to the stretching vibration of the La-O bond formed by oxidation reactions. The bond at 1135 cm^{-1} is distinct for C–O stretching typically from the esters and

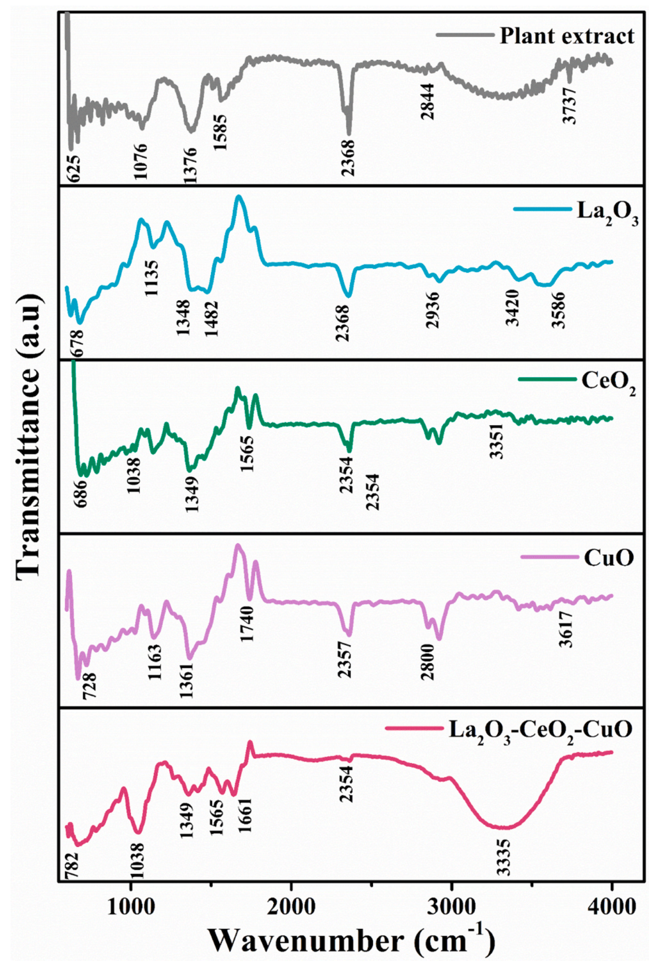

Fig. 3. FTIR patterns of *Foeniculum vulgare,* La_2O_3, CeO_2, CuO, and La_2O_3–CeO_2 -CuO.

alcohol from plant phytometabolite. A weak band at 1348 cm^{-1} and 1482 cm^{-1} is attributed to the deformation mode of OH groups. The peak is located in the region of 2368 cm^{-1}, which shows the incidence of atmospheric CO_2 in the sample. [58]. The value of the peak, ranging from 2300 to 2400 cm^{-1} is also responsible for the nitrile and cyanide group in the alkaloid metabolite of *Foeniculum vulgare*. A peak in the 2936 cm^{-1} range in *Foeniculum vulgare* synthesized is typically due to C–H stretching vibrations from organic compounds that are C–H stretching from aliphatic and aromatic plant metabolites, typically fatty acids and flavonoids. A peak in the 3420 cm^{-1} , and 3586 cm^{-1} range in is associated with O–H and N–H stretching from *Foeniculum vulgare* proteins and amines metabolites.

CeO_2 FTIR spectrum usually reveals distinctive absorption bands that correspond to different vibrational modes. The following are the main peaks frequently seen in the CeO_2 FTIR spectrum. The intense broad band observed at 686 cm^{-1} was assigned to the Ce–O bonds. The peaks observed at 1038 cm^{-1}, 1349 cm^{-1}, and 1420 cm^{-1} arise as a result of vibrational modes caused by defects, especially oxygen vacancies. Another band at 1565 cm^{-1}, 1661 cm^{-1}, and 2354 cm^{-1} represents the atmospheric moisture and centered position peaks in this range corresponding to the H-O-H bending. Weak absorbance bands in the range of 3351 cm^{-1} linked to hydroxylated in ceria surfaces (Ce–OH modes) and residue of *Foeniculum vulgare* metabolites from the synthesis process [59].

A peak in the 728 cm^{-1} range in *Foeniculum vulgare* synthesized can be attributed to M–O (Metal-Oxygen) that is Cu–O lattice vibrations in CuO. A well-defined peak appears in the region of 1163 cm^{-1} and

1361 cm^{-1}, signifying the C-O, C-N typically originating from ester, alcohol, and polyphenols. The band was observed at 1740 cm^{-1} due to the C=O stretching from Quinone, carboxylic acids, tannins, and aldehydes in *Foeniculum vulgare* metabolites. The peak is located in the region of 2357 cm^{-1}, which relates to the incidence of atmospheric CO_2 to CuO nanoparticles.

Another sharp peak in the CuO spectrum at 2800 cm^{-1}, and 2920 cm^{-1} is due to C–H stretching from fatty acids, carbohydrates, and terpenes, which originally came from the capping of plant extract. In the CuO spectrum, small peaks were observed at 3413 cm^{-1}, 3532 cm^{-1}, 3617 cm^{-1}, and 3853 cm^{-1} assigned to the -OH, -NH group originating from the plant metabolites anchoring the surface of the material.

In the La_2O_3-CeO_2-CuO nanocomposite, the metal-oxygen bond (M-O) arises at different peaks at 609 cm^{-1}, 664 cm^{-1}, 782 cm^{-1} that relate to the structural stability, and surface interaction of the nanocomposite with *Foeniculum vulgare* metabolite. Slight intense peaks were observed in the 790–1000 cm^{-1} region due to lattice distortion due to the incorporation of secondary elements of the plant that aid in the synthesis and capping. The peak around the1038cm^{-1} signifies the C-O-C, C-O stretching, and the metal phytochemical bonds due to plant flavonoids and alkaloids (M-O-C), while M represents the La, Cu, and Ce. The key vibrational assigned peaks at 1349 cm^{-1} and 1420 cm^{-1} denote the C-H bending typically (CH_2, CH_3) associated with the plant-derived metabolites of *Foeniculum vulgare*. The sharp 1565 cm^{-1} and 1661 cm^{-1} bands represent C=C and C=O stretching vibrations from flavonoids, alkaloids, lignin, and associated aromatic compounds of the plant. The peaks around 2354 cm^{-1} and 3335 cm^{-1} are assigned to different functional groups related to (C≡C) or nitriles (C≡N).

3.2. Optical properties

Using UV–visible absorption spectroscopy of the La_2O_3-CeO_2-CuO nanocomposite, the optical response of the grown pristine and nanocomposite was investigated. The findings are displayed in Fig. (4). La_2O_3, CeO_2, and CuO have absorption edges at 298 nm, 532 nm, and 503 nm, respectively. Significantly, La_2O_3–CeO_2-CuO exhibits significant absorption peaks in the visible light area at 373, 420, and 540 nm. It indicates that the nanocomposite's close interfacial contact between La_2O_3, CeO_2, and CuO produces a cumulative effect that prolongs the visible light response. To estimate the variation in energy bandgap (Eg), Tauc's plot is used [60]: (Fig. 5).

$$\alpha h\nu = A(h\nu - Eg)n \qquad (4)$$

The computed values of the energy bandgap are 4.3, 3.32, 2.3, and 2.0 eV for La_2O_3, CeO_2, and CuO and La_2O_3–CeO_2-CuO, respectively [61]. Additionally, the energy bandgap has decreased in La_2O_3–CeO_2-CuO due to the formation of a heterojunction among the La_2O_3, CeO_2, and CuO oxides, which introduces defect states and facilitates interfacial charge transfer, as reported in the literature [62–64]. The reduced bandgap implies improved visible-light absorption, electron transition, and higher visible light-harvesting capacity, all of which are beneficial for photocatalytic applications [65].

3.3. Morphology and elemental analysis

The morphology and arrangement of the nanoparticles in La_2O_3, CuO, CeO_2, and La_2O_3-CeO_2 -CuO obtained by TEM imaging. In Fig. 6 (a), La_2O_3 shows a diagonal square-shaped morphology. The CeO_2 in Fig. 6(b) showed an outgrowth of a circular sphere. The TEM image of the CuO of the sample shows almost spherical and large nanoparticles with controlled nucleation patterns, as in Fig. 6(c). The La_2O_3-CeO_2-CuO shows the agglomerated clusters forming flakes enclosing the mixtures of three oxides in a tri-phasic manner. The morphology of La_2O_3-CeO_2-CuO embedded with each other, forming a broad interface across the crystal lattice with improved catalytic properties, makes it a better candidate for biomedical and photocatalytic applications.

For the elemental composition of pristine fabricated La_2O_3, CuO, CeO_2, and La_2O_3-CeO_2-CuO nanocomposite, EDX was performed. The EDX spectrum with elemental mapping of pure and La_2O_3-CeO_2-CuO nanocomposite is displayed in Fig. 7(a-d). The pure nanoparticles La_2O_3,

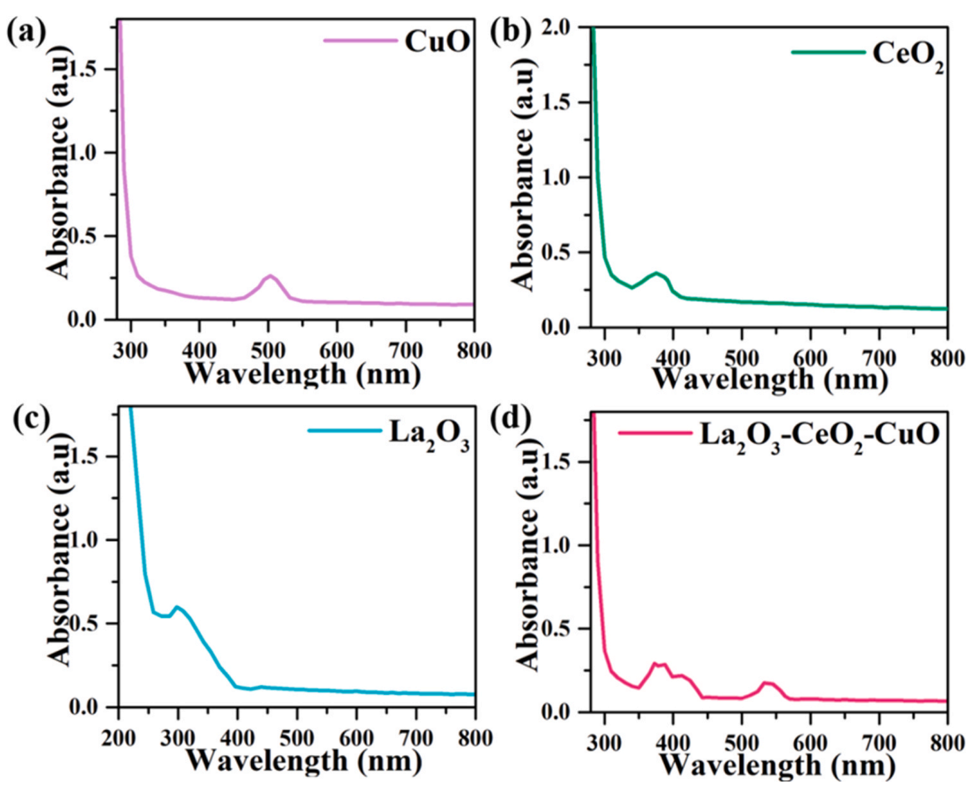

Fig. 4. UV–vis spectra of pure La_2O_3 (a), CeO_2 (b), CuO (c), and La_2O_3–CeO_2 -CuO (d).

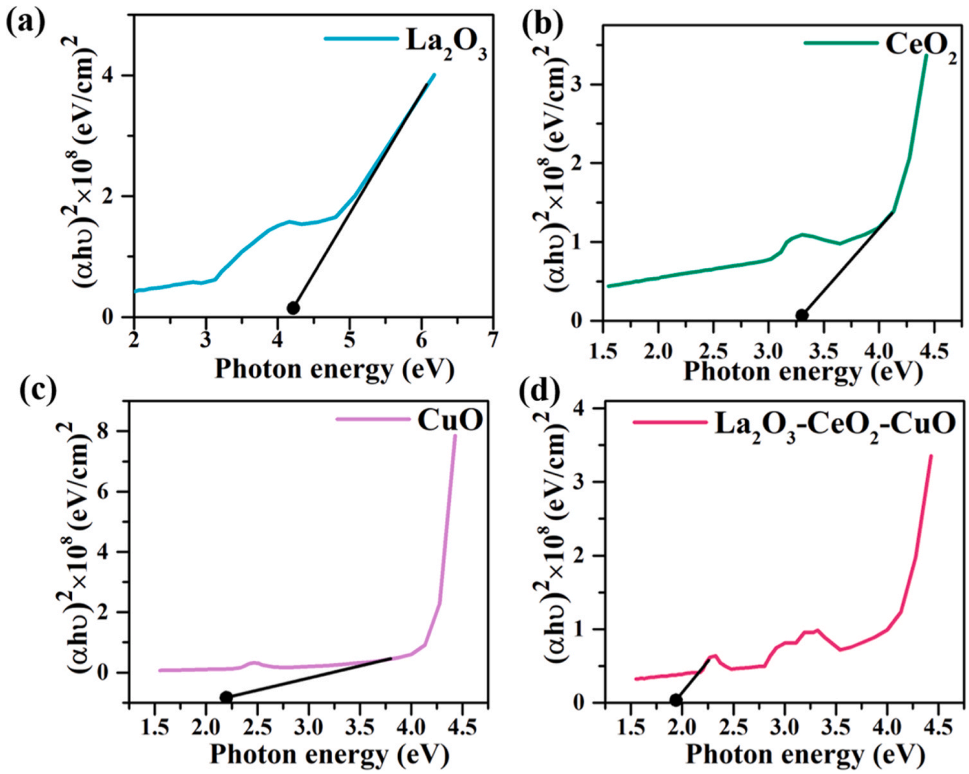

Fig. 5. Energy bandgap pattern of La_2O_3 (a), CeO_2 (b), CuO (c), and La_2O_3–CeO_2 -CuO (d).

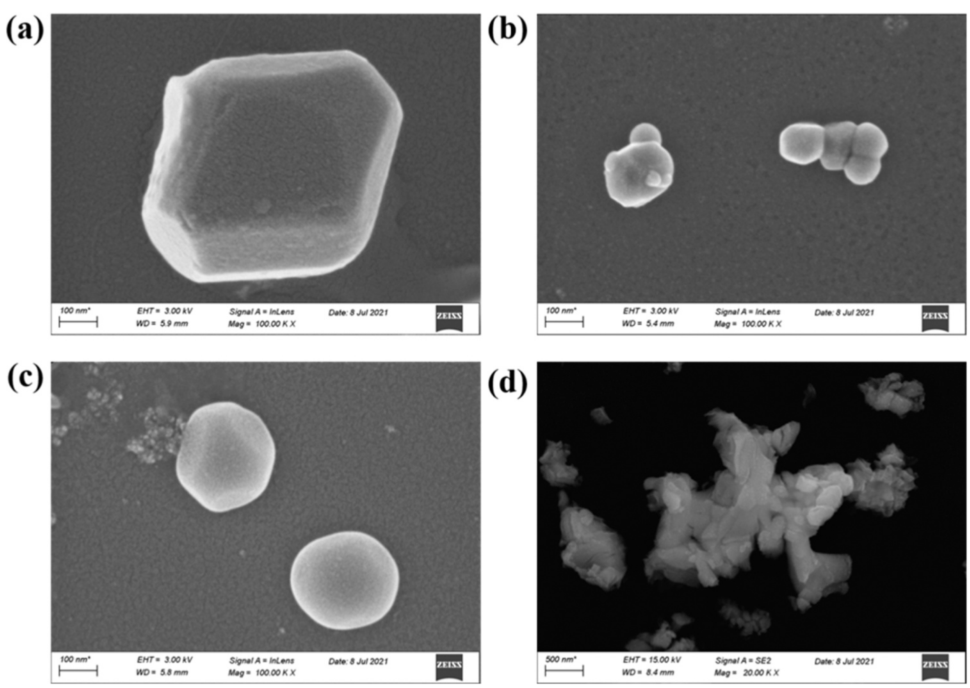

Fig. 6. TEM of pure La_2O_3, CeO_2, CuO nanoparticles, and La_2O_3–CeO_2-CuO.

CeO_2, and CuO EDX show the presence of La, Ce, and Cu, respectively. Fig reveals the uniform distribution of the lanthanum, cerium, copper, carbon, and oxygen, which were indicated with attached color mapping. The presence of La, Ce, Cu, and C elements without any other impurities is confirmed by the appearance of all the peaks of the manufactured La_2O_3, CeO_2, CuO, and La_2O_3-CeO_2-CuO sample in the EDX bands. The Edax elemental composition of La_2O_3, CuO, and CeO_2, and La_2O_3-CuO-CeO_2 is tabulated in S-6. The TEM and EDX results demonstrated an excellent *Foeniculum vulgare* assisted nanocomposite La_2O_3-CeO_2-CuO, which is beneficial for photocatalysis and anti-microbial applications.

3.4. Antimicrobial activity

The antibacterial activity of La_2O_3–CeO_2-CuO and pure La_2O_3, CeO_2,

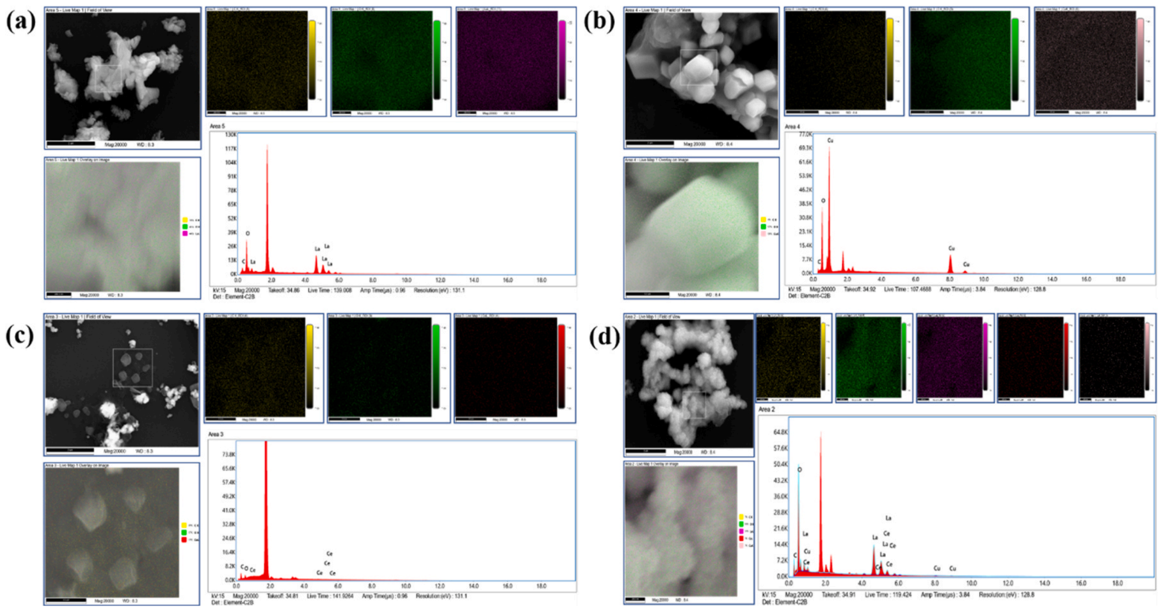

Fig. 7. EDAX Mapping of pure La_2O_3, CeO_2, CuO nanoparticles, and La_2O_3-CeO_2-CuO.

and CuO was evaluated against certain bacterial strains using the disc diffusion technique [66]. The results depicted **in** Fig. 8(a, b) demonstrated efficient activity against *E-coli* within the concentration range of 40 mg/mL, as evidenced by the zone of inhibition. The antibacterial plates of respective *S-aureus* and *E-coli* strain are shown in Fig S1, S2. In comparison, the inhibitory effect against *S-aureus* species was minimal, with a slightly smaller zone of inhibition observed. The calculated diameter of the zone of inhibition increased progressively with every enhanced dosage of La_2O_3–CeO_2 -CuO and pure La_2O_3, CeO_2, and CuO across considered bacteria [67].

The obtained outcomes verified an outstanding antibacterial potential against the tested bacteria, namely, *S. aureus* (12 ± 0.25 mm), and *E. coli* (14 ± 0.24 mm), at a concentration of 20 μg/mL for

La_2O_3. At the dosage of 40 μg/mL, La_2O_3 exposed antibacterial efficacy in contrary to *S. aureus* (13.5 ± 0.28 mm) subsequent by *E. coli* ZOI (15.3 ± 0.22 mm). When applied at 60 μg/mL, La_2O_3 showed comparatively higher inhibitory effects against *S-aureus* (15.88 ± 0.23 mm), and *E. coli* (17.45 ± 0.3 mm). The positive control ciprofloxacin showed following ZOI as *S-aureus* (28 ± 0.3 mm), and *E. coli* (27 ± 0.2 mm). CeO_2 at a concentration of 20 μg/mL showed substantial antibacterial activity against *S. aureus* (13 ± 0.5 mm), and *E. coli* (14.8 ± 0.25 mm) exhibited comparatively weaker inhibitory effects. At the dosage of 40 μg/mL, CeO_2 exhibited antibacterial activity against *S. aureus* (14.5 ± 0.5 mm), subsequent by *E. coli* ZOI (16 ± 0.5 mm). When applied at 60 μg/mL, CeO_2 showed comparatively higher inhibitory effects against *S-aureus* (17 ± 0.5 mm), and *E. coli* (19.45 ± 0.5 mm). The positive control ciprofloxacin showed following ZOI as *S-aureus* (28.5 ± 0.22 mm), and *E. coli* (29 ± 0.24 mm).

When CuO was administered at 20 μg/mL, it displayed a relatively higher antibacterial in contrary to *S. aureus* (16 ± 0.17 mm), and *E. coli* (18.8 ± 0.18 mm) than La_2O_3, CeO_2. At the dosage of 40 μg/mL, CuO exhibited antibacterial activity against *S. aureus* (17.54 ± 0.11 mm) subsequent by *E. coli* ZOI (19.23 ± 0.15 mm). When applied at 60 μg/mL, CuO showed comparatively higher inhibitory effects counter to *S-aureus* (20 ± 0.5 mm), and *E. coli* (21 ± 0.25 mm). The positive control ciprofloxacin, showed the following ZOI as *S-aureus* (29 ± 0.12 mm), and *E. coli* (30 ± 0.14 mm).

The La_2O_3-CeO_2-CuO nanocomposite showed remarkable antibacterial effects at various concentrations against *S-aureus*, and *E. coli*. At a concentration of 20 μg/mL, observed ZOI counter to *S. aureus* are (21 ± 1.1 mm), and *E. coli* (24 ± 1.0 mm). At 40 μg/mL dosage, La_2O_3–CeO_2 -CuO nanocomposite antibacterial activity counter to *S. aureus* (24 ± 0.18 mm) followed by *E. coli* ZOI (26 ± 0.15 mm). When applied at 60 μg/mL, La_2O_3–CeO_2 -CuO showed comparatively higher inhibitory effects counter to *S-aureus* (27.7 ± 0.12 mm), and *E. coli* (31.90 ± 0.15 mm). The positive control ciprofloxacin showed following ZOI as *S-aureus* (29 ± 0.19 mm), and *E. coli* (30 ± 0.12 mm).

The antibacterial properties of La_2O_3 nanoparticles were evaluated to recognize their efficacy as anti-bacterial agents. The La_2O_3 displayed percentage inhibition rates of *S-aureus* and *E. coli* at 20, 40, and 60 μg/mL is 42.86 % 48.21 % 56.71 %, and 51.85 %, 56.67 %, 64.56 %. The CeO_2 displayed percentage inhibition rates of *S-aureus* and *E. coli* at 20, 40, and 60 μg/mL is 46.43 %, 51.79 %, 60.71 % and 51.03 %, 55.17 %, 67.07 %. The CuO displayed percentage inhibition rates of *S-aureus*, and *E. coli* at 20, 40, and 60 μg/mL is 55.17 %, 60.48 %, 68.97 % and 62.67 %, 64.43 %, 70 %. The La_2O_3–CeO_2 -CuO displayed percentage inhibition rates of *S-aureus*, and *E. coli* at 20, 40, and 60 μg/mL is 70 %, 80 %, 92.33 %, and 73 %, 86.67 %, 93 %.

The potential of La_2O_3–CeO_2 -CuO in reducing bacterial viability with a maximum percentage index at 60 μg/mL, with a maximum 93 % inhibition zone against *E-coli*. The antibacterial activity of La_2O_3–CeO_2 -CuO nanocomposite at 20, 40, and 60 μg/mL was noticeable in its ability to inhibit the growth of common pathogenic bacteria, with *E-coli* being the most sensitive [66,68]. These findings suggest that La_2O_3--CeO_2-CuO could serve as an effective claimant for antimicrobial treatments. The interaction mechanism of the La_2O_3-CeO_2-CuO nanocomposite is largely influenced by its unique size and shape. The unique round spherical-shaped crystalline structure helps in its antibacterial activity [69]. The antibacterial mechanism works by the generation of reactive oxygen species (oxygenated moieties) **in** Fig. 8 **(c)**. The small size of the nanocomposite, as discussed in our XRD findings able to cross the membrane barrier. The ions produced by the nanomaterial, such as La, Ce, and Cu (positive) interact with the negatively charged membrane of bacteria. The interaction is accompanied by an electrostatic interaction, and it disrupts the membrane integrity with loss of cellular content [70]. Furthermore, *Foeniculum vulgare* derived La_2O_3-CeO_2-CuO boosts antibacterial activity by providing a bioactive phenolic, amine group, as confirmed by FTIR findings that help the nanocomposite break bacterial membranes. In the cytoplasm, the logged nanocomposite crops Reactive Oxygen Species (ROS), which creates an environment strained with oxidative stress [71]. The Reactive Oxygen Species disturb the whole cellular homeostasis and oxidation of proteins,

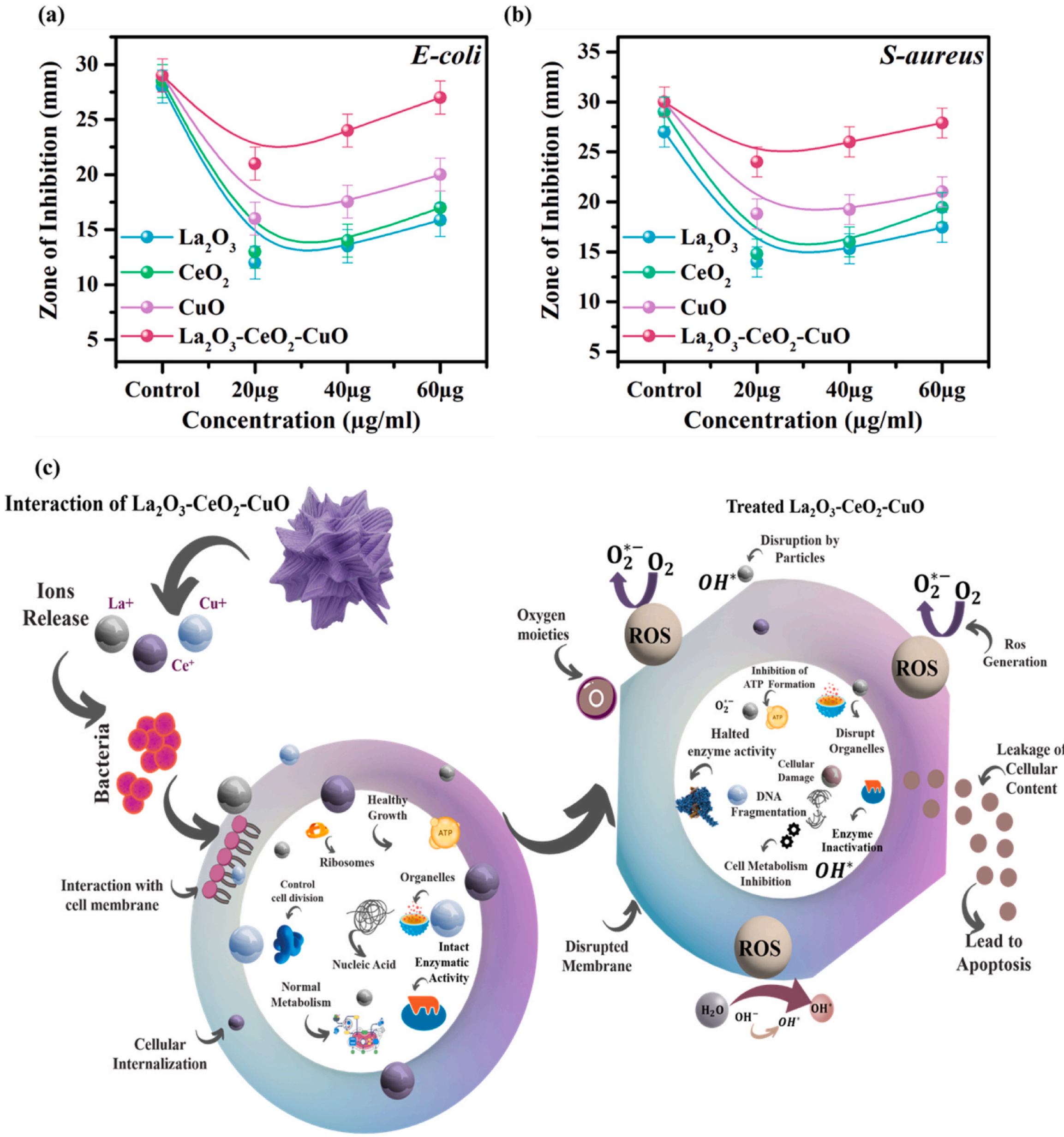

Fig. 8. Antibacterial activity of (a) *E-coli*, (b) *S-aureus* of pure La_2O_3, CeO_2, CuO nanoparticles, and La_2O_3-CeO_2-CuO and (c) Mechanism of Antibacterial action.

then lipids, and trigger mitochondrial hemorrhaging. ROS, in particular, causes major alterations such as deactivation of enzymes, along with denaturation of DNA, which eventually leads to cell death [72]. The mechanistic *Foeniculum vulgare* derivative La_2O_3-CeO_2-CuO enhances its antibacterial properties by activating these pathways. Therefore, our work proved the prospect of fabricating La_2O_3-CeO_2-CuO with considerable antibacterial activity against both gram-positive and gram-negative bacteria [73].

3.5. Photocatalysis Pathways and Mechanism

Synthetic pollutants in the form of Methylene blue dyes were used to assess the photodegradation traits of La_2O_3, CeO_2, CuO, and La_2O_3-CeO_2-CuO under solar stimulation. A prevalent organic contaminant, Methylene Blue is a dye that is cationic with a complicated molecular structure that may enter the water system via industrial effluents used to color cotton, wool, and textiles. In order to remove environmentally hazardous substances, this study uses La_2O_3, CeO_2, CuO, and La_2O_3-CeO_2-CuO to check the photodegradation efficacy of MB. Since no notable byproducts were produced during the reaction time, the degradation assessment of MB dye was carried out using UV–vis spectroscopy. The periodic progression of the absorbance spectrum changes of MB for photocatalytic experiments conducted at different times is shown in Fig. 9(a, b, c, d). The intensity of the MB characteristic absorption peak (665 nm) dropped sequentially in the presence of La_2O_3, CeO_2, and CuO catalysts, but more quickly in the presence of La_2O_3-CeO_2-CuO. After 100 min of exposure to sunlight, full degradation was attained. After the dark reaction, absorption spectrum measurements of blank dye were taken to track the role of degradation [74]. Further, a degradation pattern of MB under *Foeniculum vulgare* assisted nanocomposite was observed during regular intervals of 0, 10, 20, 40, 60, 80, and 100 min. The proportion of degradation efficiency (%) for *Foeniculum vulgare* assisted La_2O_3, CeO_2, CuO, and La_2O_3-CeO_2-CuO catalysts is depicted in Fig. 9(e). This validates that photocatalysis serves a significant part in the photodegradation reaction for MB dye eradication. The photodegradation efficiency of La_2O_3, CeO_2, CuO La_2O_3-CeO_2-CuO reaches 68 %, 73 % 91 %, 99.7 % against MB after 100 min under sunlight illumination.(Table 1)

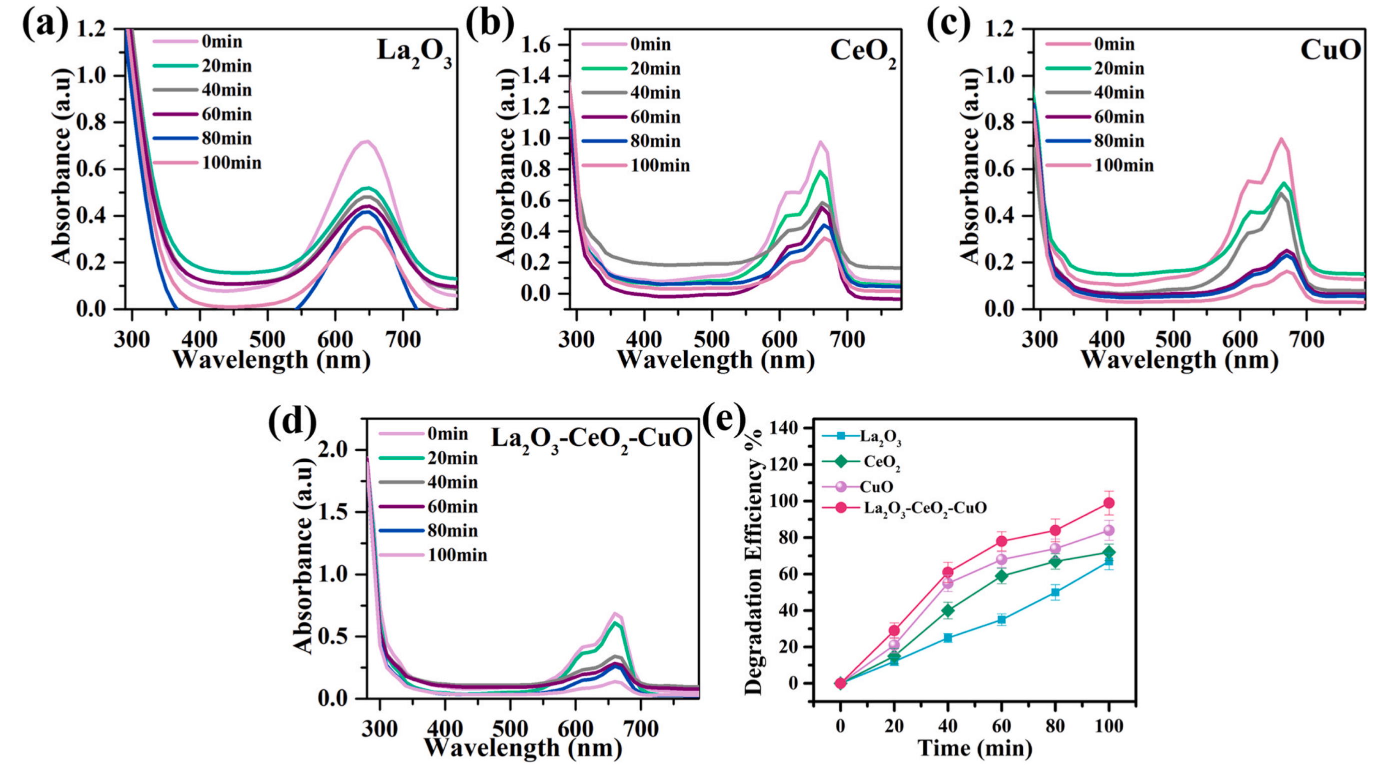

Fig. 9. Photocatalytic activity absorption spectra of pure La_2O_3, CeO_2, CuO nanoparticles, and La_2O_3–CeO_2 -CuO against MB dye (a, b, c, d), degradation efficiency (e).

Table 1
The antibacterial activity comparison with other reported nanocomposites.

Nanocomposite	Strain	ZOI	Reference
Au/MgO	***S-aureus***	19	[88]
CdS/ZnO		22	[89]
NiO·CeO_2·ZnO		14	[89]
TiO2-ZnO-MgO		15.16	[90]
CS@Ag/CeO2		16	[91]
CeO_2/GO		10.6	[92]
CeO_2-CuO-ZnO		14	[93]
Ni/ZnO		23	[94]
La_2O_3-CeO_2-CuO		27.7	Present work
Se/ZnO/CuO	***E-coli***	30.7	[95]
Cu/TiO2		25	[96]
Cu-Zn-Mn		16	[97]
g-C_3N_4/TiO_2		17	[98]
Pt/ZnO		21	[99]
Ag/V2O5-curdlan		18	[100]
GA@CuO–ZnO		21	[101]
La_2O_3-CeO_2-CuO		31.90	Present work

Moreover, the degradation process was also studied by a pseudo-first-order kinetic model, as given below [75]:

$$C_t = C_o e^{-kt} \tag{5}$$

$$=> ln(C_o/C_t) = kt \tag{6}$$

The rate constant is k. A straight line is produced by plotting the natural logarithm of concentration against various irradiation times (t), as seen in Fig. Plotting ln (Co/Ct) against irradiation time and slope yields the rate constant value. The reduction kinetics curve, ln(C0/Ct) vs. t(time)), is obtained from Fig. 10(a). Compared to individual oxide catalysts, La_2O_3-CeO_2-CuO has a higher rate constant of 0.03609 min^{-1}, (La_2O_3) 0.01126 min^{-1}, (CeO_2) 0.01456 min^{-1}, and (CuO) 0.02155 min^{-1}.(Table 2)

The higher photocatalytic performance of solar-driven photocatalysts generally requires higher separation effectiveness, redox ability, and light-capturing capacity, as depicted in Fig. 10(b) [76]. While degrading ability depends on the photocatalyst's band locations, light-capturing ability is correlated with bandgap [77]. Therefore, it is necessary to estimate the energy levels of the valence and conduction bands of the fabricated samples. The following empirical formulas were used to predict the band positions: The pathways followed by the nanocomposite are summarized in the following reactions in which the pollutant is converted into degraded products.

$$E = X - E - 0.5E \tag{7}$$

$$EV.B. = EC.B. + Eg \tag{8}$$

$$La_2O_3 + h\nu \rightarrow e^- + h^+ \tag{9}$$

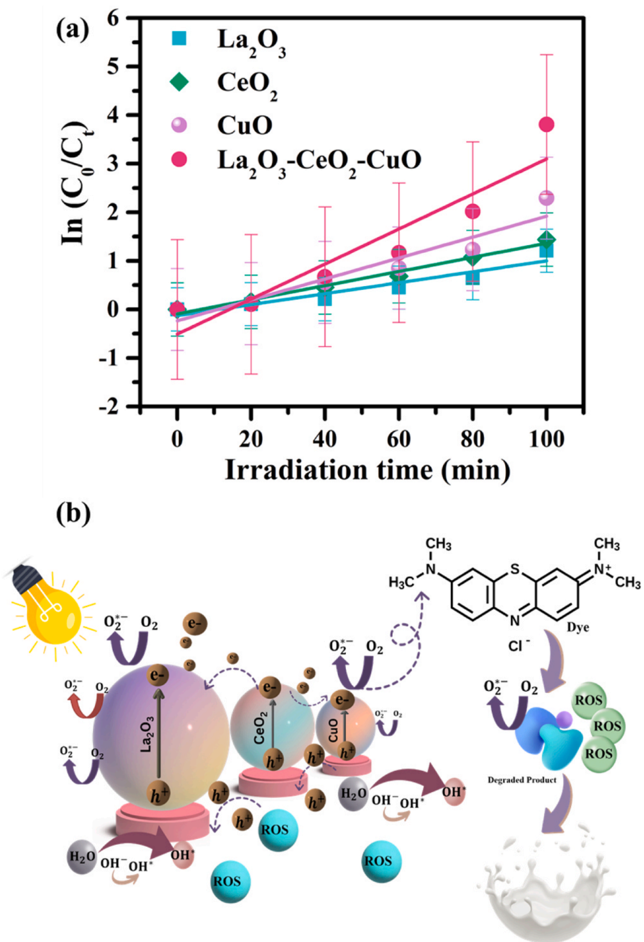

Fig. 10. Rate constant of La_2O_3, CeO_2, CuO, La_2O_3-CeO_2-CuO (a), Photocatalytic mechanism of La_2O_3, CeO_2, CuO, La_2O_3-CeO_2-CuO against MB dye (b).

$$CeO_2 + h\nu \rightarrow e^- + h^+ \quad (10)$$

$$CuO + h\nu \rightarrow e^- + h^+ \quad (11)$$

$$La_2O_3 \rightarrow CeO_2 \rightarrow CuO(\text{Conduction Band}) \quad (12)$$

$$CuO \rightarrow CeO_2 \rightarrow La_2O_3(\text{Valence Band}) \quad (13)$$

$$e^- + O_2 \rightarrow O_2^- \bullet (\text{Superoxide Radical}) \quad (14)$$

$$h^+ + H_2O \rightarrow \bullet OH + H^+(\text{Hydroxyl Radical}) \quad (15)$$

$$e^-(CB) + 2O_2 + H_2O \rightarrow H_2O_2 + e^- \rightarrow OH* \quad (16)$$

$$Dye + O_2^- \bullet / \bullet OH \rightarrow CO_2 + H_2O + Byproducts \quad (17)$$

$$La_2O_3 - CeO_2 - CuO + h\nu + O^2 + H_2O \rightarrow ROS(O^{2-}\bullet, \bullet OH) \rightarrow \text{Pollutant MB Degradation} \quad (18)$$

3.5.1. Effect of catalyst dosage

Using the appropriate amount of catalyst in the degradation of pollutants plays a crucial role. The experiment for La_2O_3-CeO_2-CuO nanocomposite was performed at different concentrations [78]. The degradation efficiency of La_2O_3-CeO_2-CuO nanocomposite catalysts having concentrations of 10, 20, 30, and 40 mg is 94.0 %, 99.5 %, 91 %, and 86 %, respectively. The photodegradation pattern of the dye under solar light irradiation can be strongly influenced by the catalyst dose of La_2O_3-CeO_2-CuO nanocomposites. Fig. 11(a) shows the degradation efficiency of La_2O_3-CeO_2-CuO nanocomposites. Results show that fabricated La_2O_3-CeO_2-CuO nanocomposites at a dose of 20 mg have supreme degradation efficiency. The 10 mg catalyst dosage has the least efficiency due to the less active site available for the catalyst and poor absorption rate. While at higher concentrations, the particle tends to agglomerate, and charge recombination increases. This is due to less diffusion of pollutant molecules to the La_2O_3-CeO_2-CuO catalyst surface.

3.5.2. Effect of pH

The wide variety of pollutants from various sectors makes it difficult to adjust pH for photocatalytic processes. There is currently no information on La_2O_3-CeO_2-CuO photocatalyst that demonstrates an effective breakdown of pollutants over a broad pH range [79]. By altering the dye solution pH, many studies looked at the impact of pH. To test the efficacy of the catalysts, the pH of the synthesized La_2O_3-CeO_2-CuO has been adjusted [80]. The characteristics of surface charge and photocatalyst aggregation are significantly influenced by pH. In the mechanistic approach of photocatalytic MB degradation, it is essential to optimize the value range at which it performs well. As the pH rises, the La_2O_3-CeO_2-CuO photocatalyst surface produces a large number of hydroxyl radicals. These radicals interact with the dye and transform into benign, less toxic moieties. It indicates that high pH levels encourage dehydrogenation, which increases MB dye elimination. La_2O_3-CeO_2--CuO nanocomposites are utilized in an alkaline environment, which exhibits comparatively higher degradation efficiencies. The photodegradation efficiency examined against various pH values of 6, 8, 10, and 12 is displayed in Fig. 11(b), with degradation efficiencies of 84, 88, 94, and 99 %, respectively. These findings confirm that the photodegradation results of plant mediated La_2O_3-CeO_2-CuO at pH = 12 have a supreme photodegradation rate. The results of La_2O_3-CeO_2-CuO clearly show that an increment in pH value intensifies the degradation efficiency.

3.5.3. Effect of dye concentrations

The degrading efficiency of La_2O_3-CeO_2-CuO nanocomposites is influenced by the initial dye concentration. Fig. 11(c). Demonstrate the degradation competence of *Foeniculum vulgare* assisted nanocomposites by varying the concentration from 20, 30, 40, and 50 ppm. The findings explicitly show that as the dye concentration increased, the degradation declined [81]. The proportion of MB degradation decreases as dye concentration rises because fewer photons access the reaction and decrease electron-hole production. Saturation of the active site occurs when significant amounts of organic contaminant molecules accumulate on the catalyst surface. The rise in dye concentration quenches the electron hole before the reaction with water and oxygen to form ROS. The formation of by-products shades the active catalytic site for the dye molecules to interact and increase the charge recombination rate. As a result, there is limited charge carrier mobility and less catalyst diffusion to the catalytic surface. To improve degradation efficiency, the photodegradation rate was thus optimized.

Table 2
Comparison table of Degradation of Methylene blue by different nanocomposite.

ZnO-CuO-graphene	Methylene Blue	81 %	[102]
ZnO/Fe_2O_3/MnO_2		93 %	[103]
CuO/ZnO	-	96.57 %	[104]
Sm_2O_3-WO_3-La_2O_3	-	99.0	[105]
TiO_2-silica	-	97.66 %	[106]
CeO_2/GO-PAM		90 %	[107]
CQDs@ZIF−8	-	93 %	[108]
AC-ZrO_2/CeO_2	-	97.91 %	[109]
CeO_2/CdS	-	98.9359 %	[110]
Ce-TiO_2/g-C_3N_4	-	93 %	[111]
Ag-doped CeO_2/ZnO	-	98.90 %	[112]
rGO/Gd_2WO_6	-	92 %	[113]
Gd_2O_3–La_2O_3	-	84.80 %	[114]
$ZnIn_2S_4$–Ag–$LaFeO_3$	-	95 %	[115]
La_2O_3-CeO_2-CuO	-	99.7 %	Present work

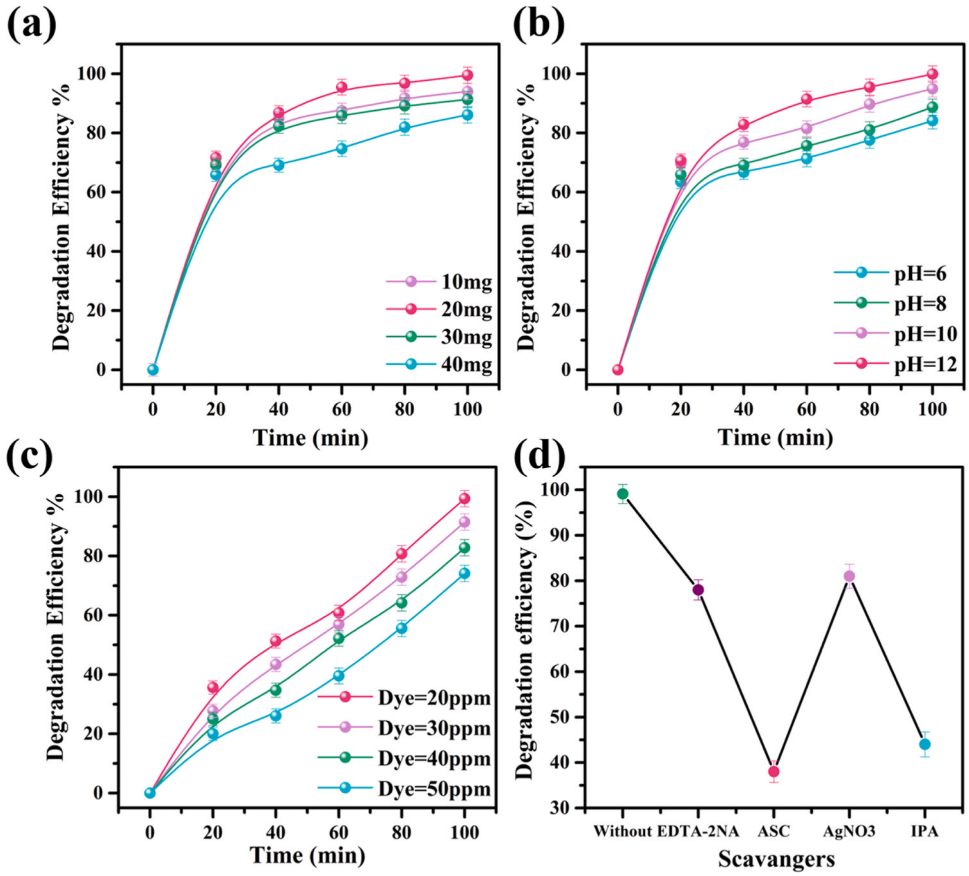

Fig. 11. Photocatalytic activity of La_2O_3-CeO_2-CuO effect on (a) catalyst dosage, (b) dye concentration, (c) pH, and scavengers (d).

3.5.4. *Scavengers experiment*

La_2O_3-CeO_2-CuO trapping studies were conducted to examine the production of reactive oxygen species that contribute to dye degradation [82,83]. Numerous studies were carried out to investigate the main reactive species, hydroxyl radical, hole, and superoxide radical anion, as well as the effect of additives on dye degradation, using a range of scavenger tests. EDTA-2Na, ASC, $AgNO_3$, and IPA are employed as scavengers in this experiment. To examine the impact of scavengers, reaction conditions were added to the solution: catalyst La_2O_3-CeO_2--CuO (20 mg) with MB-dye (10 ppm), and pH (10). The results show that the largest amount of MB dye degradation occurs in the absence of a scavenger test. Additionally, the effect of hydroxyl radicals is examined using isopropyl alcohol (IPA), and the findings indicate a considerable reduction in MB breakdown. When superoxide moieties and hydroxyl (OH) radical scavenger's cast-off instead of electron or hole scavengers, the degradation efficiency is significantly reduced. This suggests that O_2^{-}• and •OH are the main species that cause the methylene blue degradation process. Different scavengers like EDTA-2Na, ASC, $AgNO_3$, and IPA have different effects on degradation efficiency. The percentage (%) degradation efficiency without scavenger, or by adding EDTA-2Na, ASC, $AgNO_3$, and IPA was 99.1 %, 78 %, 38 %, 81 %, and 44 %, respectively, as in Fig. 11(d).

3.5.5. *Reusability test*

A multicycle MB dye degradation experiment was used to evaluate the La_2O_3-CeO_2-CuO catalyst's stability and reusability. Additionally, the stability test was assessed for seven cycles. The composite durability and reusability were demonstrated in Fig. 12(a). Throughout several

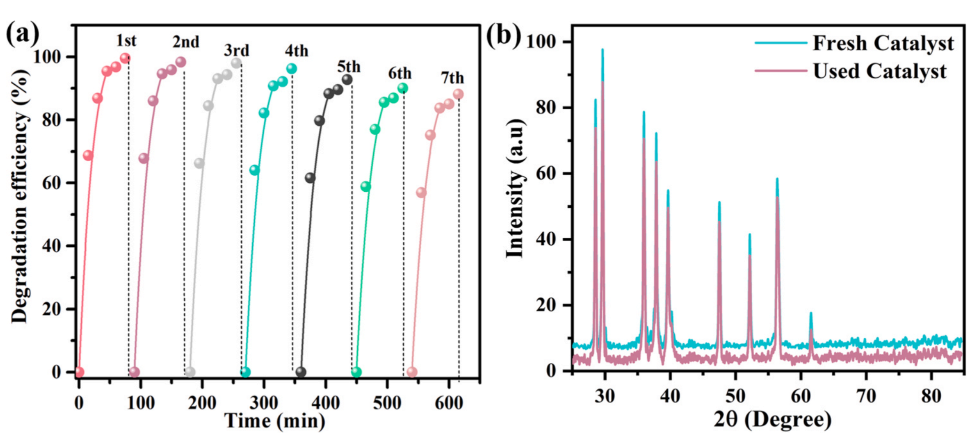

Fig. 12. Efficiency of the recycling ability of La_2O_3-CeO_2-CuO (a), XRD pattern of fresh and used catalyst La_2O_3-CeO_2-CuO (b).

cycles, the La_2O_3-CeO_2-CuO composite retained its photocatalytic activity, indicating that it may find use in wastewater treatment without undergoing noticeable performance degradation [84,85]. The La_2O_3--CeO_2-CuO photodegradation efficiencies are 99.5 % (1st), 98.34 % (2nd), 97.99 % (3rd), 96.2 % (4th), 92.74 % (5th), 91.73 % (6th), and 88.74 % (7th), as shown in Fig. 12 (a). Fig. 12 (b) shows the La_2O_3--CeO_2-CuO nanocomposite photocatalysts' XRD pattern both before and after degradation cycles. The XRD patterns of the fresh and used La_2O_3-CeO_2-CuO catalysts showed no alterations, suggesting that the crystal's nanocomposite structure remained stable throughout the cycle process. La_2O_3-CeO_2-CuO capacity to endure prolonged, repeated usage while retaining efficiency is essential for industrial applications as it increases the process's viability and cost-effectiveness [86,87].

4. Conclusion

La_2O_3-CeO_2-CuO nanocomposites and pure oxide nanostructures were successfully synthesized by the green chemistry route. The XRD, FTIR, UV-Vis, TEM, and EDAX data confirmed the formation of La_2O_3-CeO_2-CuO nanocomposites and pure oxide La_2O_3, CeO_2, CuO. The La_2O_3-CeO_2-CuO nanocomposite showed enhanced antimicrobial and photocatalytic potential compared to the pure. The photodegradation efficiency of La_2O_3-CeO_2-CuO reaches 99.7 % against MB after 100 min under sunlight illumination. The La_2O_3-CeO_2-CuO assisted microbial inhibition ability against *S-aureus, and E-coli* with maximum inhibition zone diameters 27.7 ± 0.12 mm and 31.90 ± 0.15 mm, respectively. The catalyst La_2O_3-CeO_2-CuO dose of 20 mg, dye concentration of 20 ppm, and pH 12 were optimized for maximum photodegradation. The La_2O_3-CeO_2-CuO assisted photodegradation in the absence of scavengers have the highest percentage of degradation of MB. In addition to its reusability and cyclability, this hybrid composite showed an efficient photodegradation of MB, making it appropriate for use in water purification applications. This study provides an enlightening parameter for designing highly potent antimicrobial agents. Overall, fabricated La_2O_3-CeO_2-CuO nanocomposite via *Foeniculum vulgare* proposed as an effective strategy for therapeutic and sustainable environmental remediation applications. To evaluate clinical applicability, future research should concentrate on toxicity testing, the active compound isolation, and in vivo validations.

CRediT authorship contribution statement

Calvyn Howells: Visualization, Validation, Methodology, Investigation. **Iftikhar Ahmed:** Visualization, Software, Resources, Methodology, Formal analysis. **Muhammad Saqib Saif:** Writing – original draft, Validation, Methodology, Investigation. **Muhammad Waqas:** Validation, Software, Resources, Methodology. **Tuba Tariq:** Resources, Formal analysis, Data curation, Conceptualization. **Yanjun Duan:** Methodology, Investigation, Formal analysis, Conceptualization. **Li Haitao:** Supervision, Software, Project administration, Methodology. **Mansour Ghorbanpour:** Writing – review & editing, Resources, Project administration, Investigation. **Mumtaz Hussain:** Software, Resources, Investigation, Formal analysis. **Murtaza Hasan:** Writing – review & editing, Investigation, Formal analysis, Data curation. **Sana Batool:** Resources, Methodology, Investigation, Data curation. **Ghazala Mustafa:** Writing – review & editing, Visualization, Validation, Supervision, Conceptualization.

Declaration of Competing Interest

All the authors decaled that there is no conflict of interest in this research article

Acknowledgements

We warmly thank the Department of Biotechnology, The Islamia University of Bahawalpur, Pakistan for providing space and all instruments and chemical to complete these studies.

Appendix A. Supporting information

Supplementary data associated with this article can be found in the online version at doi:10.1016/j.jece.2025.118470.

Data availability

Data will be made available on request.

References

[1] M. Tauseef, A.A. Ansari, A.H. Khoja, S.R. Naqvi, R. Liaquat, W. Nimmo, S. S. Daood, Thermokinetics synergistic effects on co-pyrolysis of coal and rice husk blends for bioenergy production, Fuel 318 (2022), https://doi.org/10.1016/j.fuel.2022.123685.

[2] D. Poggio, A. Sastraatmaja, M. Walker, S. Michailos, W. Nimmo, M. Pourkashanian, Experimental evaluation of continuous In-Situ biomethanation of CO2 in anaerobic digesters fed on sewage sludge and food waste and the influence of hydrogen Gas–Liquid mass transfer, Processes 11 (2023), https://doi.org/10.3390/pr11020604.

[3] S.M. Moghimi, A.C. Hunter, J.C. Murray, Nanomedicine: current status and future prospects, FASEB J. 19 (2005) 311–330, https://doi.org/10.1096/FJ.04-2747REV.

[4] J.D. Morris, S.S. Daood, S. Chilton, W. Nimmo, Mechanisms and mitigation of agglomeration during fluidized bed combustion of biomass: a review, Fuel 230 (2018) 452–473, https://doi.org/10.1016/j.fuel.2018.04.098.

[5] J.D. Morris, S.S. Daood, W. Nimmo, Agglomeration and the effect of process conditions on fluidized bed combustion of biomasses with olivine and silica sand as bed materials: Pilot-scale investigation, Biomass.. Bioenergy 142 (2020), https://doi.org/10.1016/j.biombioe.2020.105806.

[6] P. Mulvaney, Nanoscience vs nanotechnology-defining the field, ACS Nano 9 (2015) 2215–2217, https://doi.org/10.1021/acsnano.5b01418.

[7] Y. jie Zhao, Y. ke Zhang, Y. Cui, Y. yuan Duan, Y. Huang, G. qiang Wei, U. Mohamed, L. juan Shi, Q. Yi, W. Nimmo, Pinch combined with exergy analysis for heat exchange network and techno-economic evaluation of coal chemical looping combustion power plant with CO2 capture, Energy 238 (2022), https://doi.org/10.1016/j.energy.2021.121720.

[8] K. Al-Qayim, W. Nimmo, K. Hughes, M. Pourkashanian, Kinetic parameters of the intrinsic reactivity of woody biomass and coal chars via thermogravimetric analysis, Fuel 210 (2017) 811–825, https://doi.org/10.1016/j.fuel.2017.09.010.

[9] Y.X. Pan, Q.H. Xu, H.M. Xiao, C.Y. Li, Insights into the antibacterial activity and antibacterial mechanism of silver modified fullerene towards staphylococcus aureus by multiple spectrometric examinations, Chemosphere 342 (2023), https://doi.org/10.1016/j.chemosphere.2023.140136.

[10] Y. Deng, W. Li, L. Li, Z. Zhou, Y. Shi, R. Tang, Y. Huang, Carbon nitride in dark photocatalysis: construction, reaction mechanism, and environmental application, J. Photochem. Photobiol. C Photochem. Rev. (2025) 100711, https://doi.org/10.1016/J.JPHOTOCHEMREV.2025.100711.

[11] A. Villegas-Fuentes, A. Rosillo-de la Torre, A.R. Vilchis-Nestor, P.A. Luque, Improvement of the optical, photocatalytic and antibacterial properties of ZnO semiconductor nanoparticles using different pepper aqueous extracts, Chemosphere 339 (2023), https://doi.org/10.1016/j.chemosphere.2023.139577.

[12] S. Raissi, A. Najjari, M.K. Younes, Synthesis, characterization of zirconia doped cobalt nanoparticles (Zr doped Co-NPs) and investigation of their antibacterial activity, Mater. Chem. Phys. 308 (2023), https://doi.org/10.1016/j.matchemphys.2023.128206.

[13] F.H. Awlqadr, K.R. Majeed, A.B. Altemimi, A.M. Hassan, S.A. Qadir, M.N. Saeed, A.M. Faraj, T.H. Salih, A.J. Abd Al-Manhel, M.A.A. Najm, E. Tsakali, J.F.M. Van Impe, A.A. Abd El-Maksoud, T.G. Abedelmaksoud, Nanotechnology-based herbal Medicine: preparation, synthesis, and applications in food and Medicine, J. Agric. Food Res 19 (2025) 101661, https://doi.org/10.1016/J.JAFR.2025.101661.

[14] A.U. Khan, H.U. Khan, M.S.O. Alhar, K.Tahir Shahnaz, Z.M. Almarhoon, M.E. A. Zaki, S. Latif, A. Shah, A.U. Khan, Antimicrobial, antioxidant, and antileishmanial activity of tavernier glabra mediated ZnO NPs and Fe2O3 NPs, Inorg. Chem. Commun. 148 (2023), https://doi.org/10.1016/j.inoche.2022.110297.

[15] T. Saha, M. Bin Mobarak, M.N. Uddin, M.S. Quddus, M.R. Naim, N.S. Pinky, Biogenic synthesis of copper oxide (CuO) NPs exploiting averrhoa carambola leaf extract and its potential antibacterial activity, Mater. Chem. Phys. 305 (2023), https://doi.org/10.1016/j.matchemphys.2023.127979.

[16] X. Ji, Y. Wu, Y. Han, B. Liang, Y. Cheng, J. Zheng, S. Guo, C. Li, H. Xu, Synergistic antibacterial study of nano-Cu2O/CuO@Ag-tetracycline composites, Mater. Chem. Phys. 306 (2023), https://doi.org/10.1016/j.matchemphys.2023.127904.

[17] D.D. La, C.V. Tran, N.T.T. Hoang, M.D. Doan Ngoc, T.H.P. Nguyen, H.T. Vo, P. H. Ho, T.A. Nguyen, S.V. Bhosale, X.C. Nguyen, S.W. Chang, W.J. Chung, D. D. Nguyen, Efficient photocatalysis of organic dyes under simulated sunlight irradiation by a novel magnetic CuFe2O4@porphyrin nanofiber hybrid material fabricated via self-assembly, Fuel 281 (2020), https://doi.org/10.1016/j.fuel.2020.118655.

[18] R. Chinnasamy, K. Chinnaperumal, M. Venkatesan, K. Jogikalmat, T. Cherian, P. Willie, G. Malafaia, Eco-friendly synthesis of Ag-NPs using endostemon viscosus (Lamiaceae): antibacterial, antioxidant, larvicidal, photocatalytic dye degradation activity and toxicity in zebrafish embryos, Environ. Res 218 (2023), https://doi.org/10.1016/j.envres.2022.114946.

[19] Y. Xiao, G. Feng, G. Mustafa, M. Hasan, Improved electrocatalytic performance of TiS2 by nanohybrid with MoC nanosheets towards overall water-splitting for Green hydrogen, Fuel 393 (2025) 134993, https://doi.org/10.1016/j.fuel.2025.134993.

[20] R. Zohra, S. Meneceur, L.S. Eddine, A. Bouafia, H.A. Mohammed, G.G. Hasan, Biosynthesis and characterization of MnO2 and Zn/Mn2O4 NPs using ziziphus spina-Christi aqueous leaves extract: effect of decoration on photodegradation activity against various organic dyes, Inorg. Chem. Commun. 156 (2023), https://doi.org/10.1016/j.inoche.2023.111304.

[21] P. Panchal, D.R. Paul, A. Sharma, P. Choudhary, P. Meena, S.P. Nehra, Biogenic mediated Ag/ZnO nanocomposites for photocatalytic and antibacterial activities towards disinfection of water, J. Colloid Interface Sci. 563 (2020) 370–380, https://doi.org/10.1016/j.jcis.2019.12.079.

[22] Y. Liang, X. Lin, H. Liao, S. Gong, M. Hasan, X. Zhou, S. Gunasekaran, Bioengineering of Green rGO/Fe3O4 nanocomposites for rapid cadmium sensing and dye decomposition, Ceram. Int (2024), https://doi.org/10.1016/j.ceramint.2024.11.501.

[23] G.G. Hasan, H.A. Mohammed, M. Althamthami, A. Khelef, S.E. Laouini, S. Meneceur, Synergistic effect of novel biosynthesis SnO2@Fe3O4 nanocomposite: a comprehensive study of its photocatalytic of dyes & antibiotics, antibacterial, and antimutagenic activities, J. Photochem. Photobio. A Chem. 443 (2023), https://doi.org/10.1016/j.jphotochem.2023.114874.

[24] M. Ahmad, W. Rehman, M.M. Khan, M.T. Qureshi, A. Gul, S. Haq, R. Ullah, A. Rab, F. Menaa, Phytogenic fabrication of ZnO and gold decorated ZnO nanoparticles for photocatalytic degradation of rhodamine b, J. Environ. Chem. Eng. 9 (2021), https://doi.org/10.1016/j.jece.2020.104725.

[25] M.Y. Tahir, M. Sillanpaa, T.M. Almutairi, A.A.A. Mohammed, S. Ali, Excellent photocatalytic and antibacterial activities of bio-activated carbon decorated magnesium oxide nanoparticles, Chemosphere 312 (2023) 137327, https://doi.org/10.1016/J.CHEMOSPHERE.2022.137327.

[26] R. Kumar, K. Kumar, N. Thakur, Phyto-fabrication of CuO–Co3O4 nanocomposites for antibacterial, photocatalytic and antioxidant evaluations: an in-vitro investigation, Hybrid. Adv. 5 (2024) 100129, https://doi.org/10.1016/J.HYBADV.2023.100129.

[27] S. Kaushal, N. Thakur, K. Kumar, Investigation of the efficacy of Zn/Ce–CuO nanoparticles for enhanced photocatalytic, antibacterial, and antioxidant activities, Environ. Sci. Pollut. Res. (2024), https://doi.org/10.1007/S11356-024-34180-2.

[28] A. Sabarinathan, M. Chinnathambi, R. Jayaprakash, R. Robert, R. Uthrakumar, K. Kaviyarasu, An effective photocatalytic degradation of methylene blue with ZnO/SnO2 – CeO2/CuO quaternary nanocomposite driven by visible light irradiation, Inorg. Chem. Commun. 156 (2023) 111164, https://doi.org/10.1016/J.INOCHE.2023.111164.

[29] A.J. Aswin, M.R. Venkatraman, R. Sivasamy, B. Christopher, V. Ragavendran, G. Rajesh, Optimizing photocatalytic efficiency of La2Ti2O7 nanoparticles: a comprehensive experimental and theoretical approach, Appl. Phys. A Mater. Sci. Process 131 (2025) 1–11, https://doi.org/10.1007/S00339-025-08288-2/FIGURES/10.

[30] M. Kumar, A. Rahman, Innovations in p-n type heterostructure composite materials (La2O3/CeO2) for environmental contamination remediation: synthesis, characterization, and performance assessment, Biomass.. Convers. Biorefin 14 (2023) 23985–24006, https://doi.org/10.1007/S13399-023-04583-1/FIGURES/2.

[31] S. Karthikeyan, K. Dhanakodi, S. Surendhiran, K. Vanasundari, L. Arunraja, A. T. Rajamanickam, Unveiling the photocatalytic property of La2O3–CuO nanocomposites for organic pollutants in wastewater treatment, J. Indian Chem. Soc. 100 (2023) 101104, https://doi.org/10.1016/J.JICS.2023.101104.

[32] M. Malekkiani, F. Ravari, A. Heshmati Jannat Magham, M. Dadmehr, H. Groiss, H.A. Hosseini, R. Sharif, Fabrication of Graphene-Based TiO2@CeO2and CeO2@TiO2Core-Shell heterostructures for enhanced photocatalytic activity and cytotoxicity, ACS Omega 7 (2022) 30601–30621, https://doi.org/10.1021/acsomega.2c04338.

[33] A. G, A. P, T. P, G. V, S. G, R.K. Ramesh, P. M, Boosting the performance of solar light driven CeO2/BiVO4 anchored g-C3N4 nanocomposites: a systematic study toward the development of a photocatalytic and antibacterial activity, Colloids Surf. A Physicochem Eng. Asp. 673 (2023) 131835, https://doi.org/10.1016/J.COLSURFA.2023.131835.

[34] S.H. Hsieh, A. Manivel, G.J. Lee, J.J. Wu, Synthesis of mesoporous Bi2O3/CeO2 microsphere for photocatalytic degradation of Orange II dye, Mater. Res Bull. 48 (2013) 4174–4180, https://doi.org/10.1016/j.materresbull.2013.06.049.

[35] F. Mukhtar, T. Munawar, M.S. Nadeem, M.N. ur Rehman, S. Batool, M. Hasan, M. Riaz, K. ur Rehman, F. Iqbal, Highly efficient tri-phase TiO2–Y2O3–V2O5 nanocomposite: structural, optical, photocatalyst, and antibacterial studies, J. Nanost. Chem. 12 (2022) 547–564, https://doi.org/10.1007/S40097-021-00430-9/TABLES/5.

[36] C.M. Magdalane, K. Kaviyarasu, J.J. Vijaya, B. Siddhardha, B. Jeyaraj, Photocatalytic activity of binary metal oxide nanocomposites of CeO2/CdO nanospheres: investigation of optical and antimicrobial activity, J. Photochem. Photobio. B 163 (2016) 77–86, https://doi.org/10.1016/J.JPHOTOBIOL.2016.08.013.

[37] C. Deng, Z. Hu, S. Li, Y. Wang, G. Ma, M. Sun, M. Yaseen, L. Wang, Designing flower-like La-Bi2WO6/Ni@N-rGO composite for the photocatalytic oxidation coupled in-suit hydrogenation desulfurization of diesel oil, Fuel 358 (2024), https://doi.org/10.1016/j.fuel.2023.130283.

[38] X. Dong, J. Wang, F. Lin, J. Li, T. Yu, B. Yan, G. Chen, La0.7(Ca, Sr) 0.3Ni0.6Mn0.5O3 perovskites for photothermal catalytic reforming of toluene: the role of oxygen species in the photothermal synergistic effect, Fuel 347 (2023), https://doi.org/10.1016/j.fuel.2023.128441.

[39] S. Zeghdi, S.E. Laouini, H.A. Mohammed, A. Bouafia, M.L. Tedjani, M.M. S. Abdullah, T. Trzepieciński, Improved synthesis of Cu2O NPs and ascorbic Acid-Modified derivatives for adsorption of brilliant cresyl blue: surface and reusability studies, Materials 17 (2024), https://doi.org/10.3390/MA17102358.

[40] A.G. Bekru, L.T. Tufa, O.A. Zelekew, M. Goddati, J. Lee, F.K. Sabir, Green synthesis of a CuO-ZnO nanocomposite for efficient photodegradation of methylene blue and reduction of 4-Nitrophenol, ACS Omega 7 (2022) 30908–30919, https://doi.org/10.1021/ACSOMEGA.2C02687.

[41] B. Pant, M. Park, H.Y. Kim, S.J. Park, Ag-ZnO photocatalyst anchored on carbon nanofibers: synthesis, characterization, and photocatalytic activities, Synth. Met 220 (2016) 533–537, https://doi.org/10.1016/j.synthmet.2016.07.027.

[42] P. Goyal, S. Chakraborty, S.K. Misra, Multifunctional Fe3O4-ZnO nanocomposites for environmental remediation applications, Environ. Nanotechnol. Monit. Manag 10 (2018) 28–35, https://doi.org/10.1016/j.enmm.2018.03.003.

[43] J. Huang, B. Zhu, D. Song, B. Wang, L. Chen, L. Lu, Q. Chen, L. Gai, C. Zhai, L. Chen, H. Tao, Synergistic photocatalysis for naphthalene (NAP) removal in seawater by S-scheme heterojunction Bi2S3/CeVO4: mechanistic investigation and degradation pathways, Chem. Eng. J. 464 (2023), https://doi.org/10.1016/j.cej.2023.142784.

[44] S. Wang, W. An, J. Lu, L. Liu, J. Hu, Y. Liang, W. Cui, A Cu/CuFe2O4-OVs two-electron centre-based synergistic photocatalysis-Fenton system for efficient degradation of organic pollutants, Chem. Eng. J. 441 (2022), https://doi.org/10.1016/j.cej.2022.135944.

[45] M.A. Rather, B.A. Dar, S.N. Sofi, B.A. Bhat, M.A. Qurishi, Foeniculum vulgare: a comprehensive review of its traditional use, phytochemistry, pharmacology, and safety, Arab. J. Chem. 9 (2016) S1574–S1583, https://doi.org/10.1016/j.arabjc.2012.04.011.

[46] M. Salami, M. Rahimmalek, M.H. Ehtemam, Inhibitory effect of different fennel (Foeniculum vulgare) samples and their phenolic compounds on formation of advanced glycation products and comparison of antimicrobial and antioxidant activities, Food Chem. 213 (2016) 196–205, https://doi.org/10.1016/j.foodchem.2016.06.070.

[47] W.R. Diao, Q.P. Hu, H. Zhang, J.G. Xu, Chemical composition, antibacterial activity and mechanism of action of essential oil from seeds of fennel (Foeniculum vulgare Mill.), Food Control 35 (2014) 109–116, https://doi.org/10.1016/j.foodcont.2013.06.056.

[48] A.K. El-Sawaf, S.H. El-Moslamy, E.A. Kamoun, K. Hossain, Green synthesis of trimetallic CuO/Ag/ZnO nanocomposite using ziziphus spina-christi plant extract: characterization, statistically experimental designs, and antimicrobial assessment, Sci. Rep. 14 (2024), https://doi.org/10.1038/s41598-024-67579-5.

[49] S. Batool, M. Hasan, M. Dilshad, A. Zafar, T. Tariq, A. Shaheen, R. Iqbal, Z. Ali, T. Munawar, F. Iqbal, S.G. Hassan, X. Shu, G. Caprioli, Green synthesized ZnO-Fe2O3-Co3O4 nanocomposite for antioxidant, microbial disinfection and degradation of pollutants from wastewater, Biochem Syst. Ecol. 105 (2022), https://doi.org/10.1016/j.bse.2022.104535.

[50] T. Munawar, F. Mukhtar, M.S. Nadeem, S. Manzoor, M.N. Ashiq, K. Mahmood, S. Batool, M. Hasan, F. Iqbal, Fabrication of dual Z-scheme TiO2-WO3-CeO2 heterostructured nanocomposite with enhanced photocatalysis, antibacterial, and electrochemical performance, J. Alloy. Compd. 898 (2022), https://doi.org/10.1016/j.jallcom.2021.162779.

[51] A.K. El-Sawaf, S.H. El-Moslamy, E.A. Kamoun, K. Hossain, Green synthesis of trimetallic CuO/Ag/ZnO nanocomposite using ziziphus spina-christi plant extract: characterization, statistically experimental designs, and antimicrobial assessment, Sci. Rep. 14 (2024), https://doi.org/10.1038/s41598-024-67579-5.

[52] S. Lal, R. Verma, A. Chauhan, J. Dhatwalia, I. Guleria, S. Ghotekar, S. Thakur, K. Mansi, R. Kumar, A. Kumari, P. Kumar, Antioxidant, antimicrobial, and photocatalytic activity of Green synthesized ZnO-NPs from myrica esculenta fruits extract, Inorg. Chem. Commun. 141 (2022), https://doi.org/10.1016/j.inoche.2022.109518.

[53] D. Ayodhya, A. Ambala, G. Balraj, M. Pradeep Kumar, P. Shyam, Green synthesis of CeO2 NPs using manilkara zapota fruit peel extract for photocatalytic treatment of pollutants, antimicrobial, and antidiabetic activities, Results Chem. 4 (2022), https://doi.org/10.1016/j.rechem.2022.100441.

[54] A.M. Ismael, A.N. El-Shazly, S.E. Gaber, M.M. Rashad, A.H. Kamel, S.S.M. Hassan, Novel TiO2/GO/CuFe2O4nanocomposite: a magnetic, reusable and visible-light-driven photocatalyst for efficient photocatalytic removal of chlorinated pesticides from wastewater, RSC Adv. 10 (2020) 34806–34814, https://doi.org/10.1039/D0RA02874F.

[55] N.K. Cakmak, Z. Said, L.S. Sundar, Z.M. Ali, A.K. Tiwari, Preparation, characterization, stability, and thermal conductivity of rGO-Fe3O4-TiO2 hybrid nanofluid: an experimental study, Powder Technol. 372 (2020) 235–245, https://doi.org/10.1016/J.POWTEC.2020.06.012.

[56] S. Bibi, A. Ahmad, M.A.R. Anjum, A. Haleem, M. Siddiq, S.S. Shah, A.Al Kahtani, Photocatalytic degradation of malachite Green and methylene blue over reduced graphene oxide (rGO) based metal oxides (rGO-Fe3O4/TiO2) nanocomposite under UV–visible light irradiation, J. Environ. Chem. Eng. 9 (2021) 105580, https://doi.org/10.1016/J.JECE.2021.105580.

[57] X.S. Hu, R. Liang, G. Sun, Super-adsorbent hydrogel for removal of methylene blue dye from aqueous solution, J. Mater. Chem. A Mater. 6 (2018) 17612–17624, https://doi.org/10.1039/C8TA04722G.
[58] A. Fouda, S.E.D. Hassan, E. Saied, M.F. Hamza, Photocatalytic degradation of real textile and tannery effluent using biosynthesized magnesium oxide nanoparticles (MgO-NPs), heavy metal adsorption, phytotoxicity, and antimicrobial activity, J. Environ. Chem. Eng. 9 (2021), https://doi.org/10.1016/j.jece.2021.105346.
[59] Z. Li, L. Li, S. Zhang, L. Zhang, Y. Cui, H. Shi, Ultrasound assisted TiO2@Fe3O4 nanocomposites photocatalytic degradation of organic pollutants in potato starch processing wastewater, Sep Purif. Technol. 332 (2024), https://doi.org/10.1016/j.seppur.2023.125799.
[60] V. Sumalatha, D. Ayodhya, V. Balchander, Facile synthesis of hexagonal-shaped CuO NPs from Cu(II)-Schiff base complex for enhanced visible-light-driven degradation of dyes and antimicrobial studies, Inorg. Chim. Acta 548 (2023), https://doi.org/10.1016/j.ica.2022.121358.
[61] S. Zhang, Z. Zhang, C. Wang, S. Khan, L. Wang, R. Zhang, X. Zhang, J. Zhou, J. Duan, Coffee extract mediated Foam-Structured cerium dioxide nanoparticles: Green synthesis and enhanced photocatalytic bactericidal efficiency, Sep Purif. Technol. 361 (2025), https://doi.org/10.1016/j.seppur.2024.131310.
[62] K. Peng, L. Zhang, Y. Xie, Y. Ma, J. Ye, Y. Dai, Y. Chen, L. Wang, W. Zhang, TiO2/Bi2O2CO3 heterojunction for enhanced photocatalytic hydrogen production performance: photogenerated carrier separation, Fuel 374 (2024), https://doi.org/10.1016/J.FUEL.2024.132460.
[63] M.A. Ahmed, S.A. Mahmoud, A.A. Mohamed, Interfacially engineered metal oxide nanocomposites for enhanced photocatalytic degradation of pollutants and energy applications, RSC Adv. 15 (2025) 15561–15603, https://doi.org/10.1039/D4RA08780A.
[64] H.K. Hakki, P. Aspoukeh, H. Khojasteh, H.J. Mohammed, R. Parhaftsar, Engineering internal bandgap states and heterojunction interfaces in Chitosan-CuO-ZnO nanocomposites for superior photocatalytic degradation of direct violet 51, Surf. Interfaces 62 (2025) 106274, https://doi.org/10.1016/J.SURFIN.2025.106274.
[65] K. Kamanna, Y. Amaregouda, M.K. N, chitosan/polyvinyl alcohol-based nanocomposite films incorporated with L-Glu surface functionalized ZnO NPs: physicochemical, photocatalytic, antimicrobial and antioxidant properties evaluation, Environ. Nanotechnol. Monit. Manag 20 (2023), https://doi.org/10.1016/j.enmm.2023.100861.
[66] A. Demirbas, V. Yilmaz, N. Ildiz, A. Baldemir, I. Ocsoy, Anthocyanins-rich berry extracts directed formation of ag NPs with the investigation of their antioxidant and antimicrobial activities, J. Mol. Liq. 248 (2017) 1044–1049, https://doi.org/10.1016/j.molliq.2017.10.130.
[67] N. Akhtar, C. Choi, M. Ateeq, P. Fazil, N.S. Shah, J.A. Khan, A.G. Al-Sehemi, A. Zada, M.I. Ali Shah, R. Ikram, C. Han, Visible light active CdS/CuO nanocomposites for photocatalytic degradation of ciprofloxacin, H2 production and antimicrobial activity, Chem. Eng. J. 507 (2025), https://doi.org/10.1016/j.cej.2025.160336.
[68] M.A. Ansari, S.M.M. Asiri, Green synthesis, antimicrobial, antibiofilm and antitumor activities of superparamagnetic γ-Fe2O3 NPs and their molecular docking study with cell wall mannoproteins and peptidoglycan, Int J. Biol. Macromol. 171 (2021) 44–58, https://doi.org/10.1016/j.ijbiomac.2020.12.162.
[69] M. Abu-Dalo, A. Jaradat, B.A. Albiss, N.A.F. Al-Rawashdeh, Green synthesis of TiO2 NPs/pristine pomegranate peel extract nanocomposite and its antimicrobial activity for water disinfection, J. Environ. Chem. Eng. 7 (2019), https://doi.org/10.1016/j.jece.2019.103370.
[70] C. Song, S. Luo, M. He, X. Zhao, M. Sun, Antibacterial mechanism of water-soluble CeO2 nanoflowers and its product design in antibacterial application, Appl. Surf. Sci. 679 (2025), https://doi.org/10.1016/j.apsusc.2024.161249.
[71] I.M. El-Nahhal, J. Salem, F.S. Kodeh, A. Elmanama, R. Anbar, CuO–NPs, CuO–Ag nanocomposite and Cu(II)-curcumin complex coated cotton/starched cotton antimicrobial materials, Mater. Chem. Phys. 285 (2022), https://doi.org/10.1016/j.matchemphys.2022.126099.
[72] S.L. Banerjee, M. Khamrai, K. Sarkar, N.K. Singha, P.P. Kundu, Modified chitosan encapsulated core-shell ag nps for superior antimicrobial and anticancer activity, Int J. Biol. Macromol. 85 (2016) 157–167, https://doi.org/10.1016/j.ijbiomac.2015.12.068.
[73] X. Zhang, C. Li, F. Yuan, S. Zheng, Z. Sun, Preparation and carrier preference of synergistic antibacterial cetylpyridinium/Cu2+/halloysite composite, Appl. Surf. Sci. 681 (2025), https://doi.org/10.1016/j.apsusc.2024.161519.
[74] N. Zhang, S. Peng, Z. Liu, Y. Li, J. Huang, J. Li, H. Wan, S. Zhou, Z. Gao, T. Chen, Ag NPs decorated on the magnetic Fe3O4@PDA as efficient catalyst for organic pollutants removal and as effective antimicrobial agent for microbial inhibition, J. Alloy. Compd. 928 (2022), https://doi.org/10.1016/j.jallcom.2022.167257.
[75] Z. Nasir, M.L. Shakir, R. Wahab, M. Shoeb, P. Alam, R.H. Khan, M. Mobin, Co-precipitation synthesis and characterization of co doped SnO2 NPs, HSA interaction via various spectroscopic techniques and their antimicrobial and photocatalytic activities, Int J. Biol. Macromol. 94 (2017) 554–565, https://doi.org/10.1016/j.ijbiomac.2016.10.057.
[76] M. Li, X. Sun, H. Wang, Y. Liu, F. Pan, Z. Wang, Y. Li, C. Qin, Synthesis and mechanism of hierarchical porous Ag/CuxO (x = 1, 2) nanowire hybrids for high photocatalytic degradation, Appl. Surf. Sci. 670 (2024), https://doi.org/10.1016/j.apsusc.2024.160648.
[77] N. González-Ballesteros, P.M. Martins, C.J. Tavares, S. Lanceros-Méndez, Quercetin-mediated Green synthesis of Au/TiO2 nanocomposites for the photocatalytic degradation of antibiotic ciprofloxacin, J. Ind. Eng. Chem. (2024), https://doi.org/10.1016/j.jiec.2024.09.003.
[78] Q. Zhan, Y. Fu, G. Feng, M.M. Ahmed, Q. Liu, G. Mustafa, M. Hasan, Green engineered Mo-CeO2@C nanocomposites for visible light-assisted dye decomposition and microbial apoptosis, Ceram. Int (2024), https://doi.org/10.1016/j.ceramint.2024.09.086.
[79] F. Mukhtar, T. Munawar, M.S. Nadeem, M. Naveed ur Rehman, S.A. Khan, M. Koc, S. Batool, M. Hasan, F. Iqbal, Dual Z-scheme core-shell PANI-CeO2-Fe2O3-NiO heterostructured nanocomposite for dyes remediation under sunlight and bacterial disinfection, Environ. Res 215 (2022), https://doi.org/10.1016/j.envres.2022.114140.
[80] B. Sharma, M.A. Majeed Khan, S. Rani, R.M. Singh, S. Kumar, Hydrothermal synthesis of AgNWs/rGO nanocomposite and its effective photocatalytic performance for degradation of organic pollutants, Materials Science Engineering B 313 (2025), https://doi.org/10.1016/j.mseb.2025.117987.
[81] Z. Ganbarpour, M. Mirshafiei, M. Pourmadadi, F. Yazdian, H. Rashedi, A. Rahdar, S. Fathi-karkan, S. Pandey, Revolutionizing dye degradation: enhanced photocatalytic performance of CQDs-Mg-ZnO nanocomposites via RSM optimization, Bionanoscience 15 (2025), https://doi.org/10.1007/s12668-024-01738-w.
[82] O. Havelka, S. Abdallah, J. Braun, B.K. Raczak, S. Wacławek, D. Łukowiec, R. Torres-Mendieta, Laser-synthesized FeBi nanoparticles for the efficient photocatalytic degradation of persistent antibiotics in water, J. Water Process Eng. 69 (2025), https://doi.org/10.1016/j.jwpe.2024.106706.
[83] M. Elahian, N. Ahmadi, A.A. Heidari, N. Mengelizadeh, D. Balarak, Preparation of a polyaniline-supported Ce-Ag-doped ZnO nanocomposite for efficient photocatalytic degradation of acid blue 113 dye, Results Eng. 25 (2025), https://doi.org/10.1016/j.rineng.2024.103824.
[84] A. Khan, H.Y. Chen, C. Rusly, Visible-light-driven removal of mixed dye pollutants by a novel ZnO/CNT/GO ternary nanocomposite: synergistic degradation of Congo red and methylene blue, Environ. Res 283 (2025) 122156, https://doi.org/10.1016/J.ENVRES.2025.122156.
[85] P. Jangra, P. Kumari, S.K. Sharma, K. Yadav, C. Devi, G.K. Yogesh, Synthesis, characterization, and photocatalytic degradation of methylene blue dye using Bi2S3/WS2/gC3N4-based heterojunction nanocomposite, Mater. Sci. Semicond. Process 197 (2025) 109710, https://doi.org/10.1016/J.MSSP.2025.109710.
[86] S. Vidhya, Y. Subramanian, J. Gajendiran, S.G. Raj, B.S. Bharath, A. Durairajan, M.T. Le, U. Mamudu, G.R. Kumar, J.K. Kumar, Methylene blue dye degradation characteristics of BiFeO3-graphene-LiNbO3 ternary nanocomposites, Sustain. Mater. Technol. 44 (2025) e01331, https://doi.org/10.1016/J.SUSMAT.2025.E01331.
[87] N.P. Lata, Md.S. Hussain, Md Abdulla-Al-Mamun, T.U. Rashid, S.Md Shamsuddin, Fabrication and synergistically enhanced photocatalytic activity of ternary kaolinite, TiO2, and Al2O3 (K65T30A5) nanocomposite for visible-light-induced degradation of methylene blue and remazol red dye, Heliyon 10 (2024) e29255, https://doi.org/10.1016/J.HELIYON.2024.E29255.
[88] A.U. Khan, Q.U. Khan, K. Tahir, S. Ullah, A. Arooj, B. Li, K. ur Rehman, S. Nazir, M.U. Khan, I. Ullah, A tagetes minuta based eco-benign synthesis of multifunctional Au/MgO nanocomposite with enhanced photocatalytic, antibacterial and DPPH scavenging activities, Mater. Sci. Eng. C. 126 (2021), https://doi.org/10.1016/j.msec.2021.112146.
[89] M.A. Subhan, T. Ahmed, N. Uddin, A.K. Azad, K. Begum, Synthesis, characterization, PL properties, photocatalytic and antibacterial activities of nano multi-metal oxide NiO·CeO2·ZnO, Spectrochim. Acta A Mol. Biomol. Spectrosc. 136 (2015) 824–831, https://doi.org/10.1016/j.saa.2014.09.100.
[90] L.M. Anaya-Esparza, E. Montalvo-González, N. González-Silva, M.D. Méndez-Robles, R. Romero-Toledo, E.M. Yahia, A. Pérez-Larios, Synthesis and characterization of TiO2-ZnO-MgO mixed oxide and their antibacterial activity, Materials 12 (2019), https://doi.org/10.3390/ma12050698.
[91] F.B. Kayani, S. Rafique, R. Akram, M. Hussain, K. Raja, J.S. Khan, Fabrication of novel chitosan@Ag/CeO2 hybrid nanocomposites for the study of antibacterial activity, Phys. E Low. Dimens Syst. Nanostruct. 149 (2023), https://doi.org/10.1016/j.physe.2023.115683.
[92] G. Sharma, D. Prema, K.S. Venkataprasanna, J. Prakash, S. Sahabuddin, G. Devanand Venkatasubbu, Photo induced antibacterial activity of CeO2/GO against wound pathogens, Arab. J. Chem. 13 (2020) 7680–7694, https://doi.org/10.1016/j.arabjc.2020.09.004.
[93] M.A. Subhan, N. Uddin, P. Sarker, A.K. Azad, K. Begum, Photoluminescence, photocatalytic and antibacterial activities of CeO2·CuO·ZnO nanocomposite fabricated by co-precipitation method, Spectrochim. Acta A Mol. Biomol. Spectrosc. 149 (2015) 839–850, https://doi.org/10.1016/j.saa.2015.05.024.
[94] M.S.O. Alhar, D. Muhammad, K. Tahir, M.E.A. Zaki, M. Urooj, S. Nazir, K. Albalawi, H.S. Al-Shehri, E.A.M. Saleh, A.U. Khan, An Eco-Benign biomimetic approach for the synthesis of Ni/ZnO nanocomposite: photocatalytic and antioxidant activities, Molecules 28 (2023), https://doi.org/10.3390/molecules28041705.
[95] M.A. Amin, N.A. Algamdi, M.S. Waznah, D.A. Bukhari, S.M. Alsharif, F. Alkhayri, M. Abdel-Nasser, A. Fouda, An insight into antimicrobial, antioxidant, anticancer, and antidiabetic activities of trimetallic Se/ZnO/CuO nanoalloys fabricated by aqueous extract of nitraria retusa, J. Clust. Sci. 36 (2025), https://doi.org/10.1007/s10876-024-02742-6.
[96] Y. Miao, X. Xu, K. Liu, N. Wang, Preparation of novel Cu/TiO2 mischcrystal composites and antibacterial activities for escherichia coli under visible light, Ceram. Int 43 (2017) 9658–9663, https://doi.org/10.1016/j.ceramint.2017.04.137.
[97] M.W. Alam, H.S. Al Qahtani, B. Souayeh, W. Ahmed, H. Albalawi, M. Farhan, A. Abuzir, S. Naeem, Novel Copper-Zinc-Manganese ternary metal oxide

nanocomposite as heterogeneous catalyst for glucose sensor and antibacterial activity, Antioxidants 11 (2022), https://doi.org/10.3390/antiox11061064.

[98] V. Shanmugam, S. Sanjeevamuthu, K.S. Jeyaperumal, R. Vairamuthu, Fabrication of heterostructured vanadium modified g-C 3 n 4 /TiO 2 hybrid photocatalyst for improved photocatalytic performance under visible light exposure and antibacterial activities, J. Ind. Eng. Chem. 76 (2019) 318–332, https://doi.org/10.1016/j.jiec.2019.03.056.

[99] K. ur Rehman, K. Tahir, H.A. AL-Abdulkarim, E.A.M. Saleh, A.M. Alosaimi, M. A. Hussein, A.U. Khan, Z.U.H. Khan, S. Nazir, U. Zaman, Photoinhibition and photocatalytic response of surfactant mediated Pt/ZnO nanocomposite, Photo Photo Ther. 35 (2021), https://doi.org/10.1016/j.pdpdt.2021.102458.

[100] Y.A. Shaban, M.I. Orif, M.A. Ghandourah, A.J. Turki, H.S. Alorfi, M. Al-Boqami, H.I. Althagbi, W.M. Alarif, Green synthesis of Ag/V2O5 and Ag/V2O5-curdlan nanocomposites from sargassum latifolium extract for enhanced antimicrobial and antioxidant activities, Int. J. Biol. Macromol. 301 (2025), https://doi.org/10.1016/j.ijbiomac.2025.140472.

[101] G.S. El-Sayyad, E.S.R. El-Sayed, S.H. Rizk, M.A. Abdel-Maksoud, A.M. Zakri, A. Malik, M.N. Malash, A.H. Hashem, An eco-friendly and cost-effective approach for the synthesis of a novel GA@CuO-ZnO nanocomposite: characterization, antimicrobial and anticancer activities, RSC Adv. 15 (2025) 513–523, https://doi.org/10.1039/d4ra04312j.

[102] H. Rashid, E. Muhammad, M. Hassan, A. Rauf, A. Bashir, W. Ali, T. Jan, A. Bahadur, S. Iqbal, S. Mahmood, K.M. Alotaibi, Synthesis, structural and photocatalytic properties of ZnO-CuO, ZnO-Graphene and ZnO-CuO-Graphene nanocomposites, Polyhedron 273 (2025), https://doi.org/10.1016/j.poly.2025.117471.

[103] H. Tedla, I. Díaz, T. Kebede, A.M. Taddesse, Synthesis, characterization and photocatalytic activity of zeolite supported ZnO/Fe2O3/MnO2 nanocomposites, J. Environ. Chem. Eng. 3 (2015) 1586–1591, https://doi.org/10.1016/j.jece.2015.05.012.

[104] P. Bharathi, S. Harish, J. Archana, M. Navaneethan, S. Ponnusamy, C. Muthamizhchelvan, M. Shimomura, Y. Hayakawa, Enhanced charge transfer and separation of hierarchical CuO/ZnO composites: the synergistic effect of photocatalysis for the mineralization of organic pollutant in water, Appl. Surf. Sci. 484 (2019) 884–891, https://doi.org/10.1016/j.apsusc.2019.03.131.

[105] T. Munawar, M. Shahid Nadeem, F. Mukhtar, S. Manzoor, M. Naeem Ashiq, S. Batool, M. Hasan, F. Iqbal, Multifunctional dual Z-scheme heterostructured Sm2O3-WO3-La2O3 nanocomposite: enhanced electrochemical, photocatalytic, and antibacterial properties, Adv. Powder Technol. 34 (2023), https://doi.org/10.1016/j.apt.2023.104061.

[106] L.T. Popoola, A.S. Yusuff, A.T. Adejare, S.B. Olasupo, Photocatalytic degradation of methylene blue dye by magnetized TiO2-silica nanoparticles from rice husk, Appl. Water Sci. 14 (2024), https://doi.org/10.1007/s13201-023-02052-8.

[107] Z. Kalaycıoğlu, B. Özuğur Uysal, Ö. Pekcan, F.B. Erim, Efficient photocatalytic degradation of methylene blue dye from aqueous solution with cerium oxide nanoparticles and graphene Oxide-Doped polyacrylamide, ACS Omega 8 (2023) 13004–13015, https://doi.org/10.1021/acsomega.3c00198.

[108] A.A. Abd El Khalk, M.A. Betiha, A.S. Mansour, M.G. Abd El Wahed, A.M. Al-Sabagh, High degradation of methylene blue using a new nanocomposite based on zeolitic imidazolate Framework-8, ACS Omega 6 (2021) 26210–26220, https://doi.org/10.1021/acsomega.1c03195.

[109] X. Zhang, A. Sathiyaseelan, L. Zhang, Y. Lu, T. Jin, M.H. Wang, Zirconium and cerium dioxide fabricated activated carbon-based nanocomposites for enhanced adsorption and photocatalytic removal of methylene blue and tetracycline hydrochloride, Environ. Res 261 (2024), https://doi.org/10.1016/j.envres.2024.119720.

[110] M. Danish, H. Ayub, Z.A. Sandhu, A. Shoaib, S. Akram, J. Najeeb, S. Naeem, Synthesis of cerium oxide/cadmium sulfide nanocomposites using inverse microemulsion methodology for photocatalytic degradation of methylene blue, Appl. Nanosci. 11 (2021) 2503–2515, https://doi.org/10.1007/s13204-021-02027-8.

[111] S. Nallusamy, S. Asaithambi, S. Pandiaraj, M. Rahaman, V. Elangovan, N. Eswaramoorthy, C. Nandagopal, Cerium-modified TiO2/g-C3N4 nanocomposites with synergistic effect on enhancing visible-light photocatalytic activity employing cationic dyes, Colloids Surf. A Physicochem Eng. Asp. 685 (2024), https://doi.org/10.1016/j.colsurfa.2024.133175.

[112] G.X. Wan, Y. Feng, F.F. Zhang, X.W. Sun, Y.X. Li, R.J. Xue, Hydrothermal synthesis of ag doped ZnO/CeO2 nanocomposites and its application in ethanol sensing, Mater. Lett. 318 (2022), https://doi.org/10.1016/j.matlet.2022.132191.

[113] V. Raja, K. Kuppusamy, Synthesis and characterization of rGO/Gd2WO6 nanocomposite for efficient photocatalytic degradation of organic pollutant's and antioxidant's activity, Res. Chem. Intermed. (2025), https://doi.org/10.1007/s11164-025-05521-8.

[114] S. Chandrasekar, N. Ambikapathi, P. Inbaraj, Q. Jing, B. Liu, Harvesting high-performance electro-water oxidation and selective MB degradation through dual functional Gd2O3–La2O3 photo-electrocatalysts, Mater. Today Sustain. 27 (2024), https://doi.org/10.1016/j.mtsust.2024.100947.

[115] D. Jia, J. Pan, D. Zhang, M. Wang, Y. Li, Construction of novel spherical ZnIn2S4–Ag–LaFeO3 heterostructures for enhancing photocatalytic efficiency, J. Rare Earths (2024), https://doi.org/10.1016/j.jre.2024.02.002.